remote sensing

MDPI

Article

Continuous Monitoring and Improvement of the Blasting Process in Open Pit Mines Using Unmanned Aerial Vehicle Techniques

Thomas Bamford *, Filip Medinac and Kamran Esmaeili

Department of Civil & Mineral Engineering, University of Toronto, Toronto, ON M5S1A4, Canada; filip.medinac@alum.utoronto.ca (F.M.); kamran.esmaeili@utoronto.ca (K.E.)

* Correspondence: thomas.bamford@mail.utoronto.ca

Received: 9 July 2020; Accepted: 24 August 2020; Published: 29 August 2020

Abstract: The current techniques used for monitoring the blasting process in open pit mines are manual, intermittent and inefficient and can expose technical manpower to hazardous conditions. This study presents the application of unmanned aerial vehicle (UAV) systems for monitoring and improving the blasting process in open pit mines. Field experiments were conducted in different open pit mines to assess rock fragmentation, blast-induced damage on final pit walls, blast dynamics and the accuracy of blastholes including production and pre-split holes. The UAV-based monitoring was done in three different stages, including pre-blasting, blasting and post-blasting. In the pre-blasting stage, pit walls were mapped to collect structural data to predict in situ block size distribution and to develop as-built pit wall digital elevation models (DEM) to assess blast-induced damage. This was followed by mapping the production blasthole patterns implemented in the mine to investigate drillhole alignment. To monitor the blasting process, a high-speed camera was mounted on the UAV to investigate blast initiation, sequencing, misfired holes and stemming ejection. In the post-blast stage, the blasted rock pile (muck pile) was monitored to estimate fragmentation and assess muck pile configuration, heave and throw. The collected aerial data provide detailed information and high spatial and temporal resolution on the quality of the blasting process and significant opportunities for process improvement. The current challenges with regards to the application of UAVs for blasting process monitoring are discussed, and recommendations for obtaining the most value out of an UAV application are provided.

Keywords: mining; pit wall surveying; blasting; digital photogrammetry; unmanned aerial vehicle; drone

1. Introduction

Blasting is a key activity in the mining cycle, commonly used in both open pit and underground mines to fragment the rock mass into rock boulders that can be handled by mine equipment. The resulting range of blasted block size distribution (BBSD) has important implications on downstream processes, including the energy consumption and productivity of crushing and grinding systems [1,2]. The blasting process is usually adjusted to achieve a target BBSD that can holistically minimize the overall cost of mining and milling [1,3]. The blast-induced fragmentation process is affected by the block sizes of the in situ rock mass, called the in situ block size distribution (IBSD). Rock masses with a smaller IBSD usually obtain a smaller target BBSD when blast design is constant [4]. Achieving a desired BBSD requires a comprehensive quality assurance/quality control (QA/QC) procedure to ensure that the blasting parameters are accurately implemented in the field [5,6]. This entails monitoring of the blast location and assessing the blasting pattern's compliance with the

designed pattern. Current blast assessment is often performed based on measurement of the blast design parameters and the final resulting rock pile (muck pile). Limited efforts are made in mining operations to monitor the blast dynamics, including the blast sequencing process, and diagnosing the sources of poor compliance between desired blast outcome and the actual blasted muck pile. Terrestrial high-speed cameras are generally used to monitor blast dynamics in open pit mines [7]. While achieving the target fragmentation is important, it is critical to minimize damage to the final pit walls. With reduced damage to the final pit walls, the mining operation can achieve the desired final wall geometry and can steepen the pit slope angles. This has both safety and economic implications: minimizing overbreak improves structural integrity and stability, while also reducing waste rock removal [8,9]. The current techniques used for monitoring and assessing the blasting process in open pit mines are manual, discontinuous and intermittent. These methods hinder timely and efficient decision-making and limit improvement opportunities. Moreover, the manual and terrestrial monitoring techniques can expose personnel to hazardous conditions such as falling rocks, loose ground and sharing workspace with heavy equipment. A continuous process control and feedback are required to better manage and improve the blasting process in mining operations.

In recent years, the use of unmanned aerial vehicles (UAVs) has increased significantly in various open pit mining applications [10–15]. The use of terrestrial remote sensing techniques, such as photogrammetry and LiDAR, has also increased over the last decade; however, one of the major limitations with terrestrial remote sensing is the presence of occlusions [16]. Occlusions are areas not exposed for remote sensing, either due to the setup geometry or the presence of material blocking the sight. Additionally, many of the safety concerns involved with structural mapping and fragmentation analysis have been alleviated by remote sensing because it reduces the exposure to hazardous field conditions for mine personnel. Mine personnel can avoid conducting structural mapping along the base of a bench. Using UAVs can address occlusions while maintaining safety. Furthermore, UAV systems can obtain closer access to the rock mass or blasted rock piles, thereby increasing the potential resolution of the models generated. Using high quality aerial sensing data (e.g., 2D images, high-speed video footage) together with image analysis techniques and digital photogrammetry allows for the development of a continuous and intelligent monitoring system for the blasting process in mining operations. Except for a few studies that illustrate the applications of UAVs for structural pit wall mapping [17], rock fragmentation analysis [12], assessment of drillhole alignment [18] and dust monitoring [19], using UAVs and sensing technology to address blasting process monitoring has not been extensively studied.

This study aims to present UAV solutions for blasting process monitoring and improvement in open pit mine operations. The applications, advantages and limitations of UAV and sensing technologies for blasting process monitoring are discussed. This includes structural mapping, IBSD estimation, assessment of drillhole alignment, monitoring blast dynamics using high-speed cameras, assessing blast fragmentation and blast impact on final pit walls, quality control of pre-split drillholes and assessing the broken rock pile (muck pile) configuration. UAV systems were used to collect data at four open pit mine sites: one located in Central America (Mine A), two located in North America (Mines B and D) and one in Africa (Mine C). Mine A primarily produces gold with some silver by-product. It is set in a volcanic series, dominated by rocks of andesitic composition. It is located along a northeast structural trend with mineralization hosted within numerous sub-structures, consisting of quartz stockwork, breccia and vein mineralization. Mine B is a quarry that mines limestone for the production of cement, aggregate and building stone. It has well developed vertical jointing, as well as horizontal bedding planes. Mines C and D both produce gold. Mine C is hosted within a Precambrian greenstone belt. Its deposits are strongly folded and sheared, contributing to significant foliation. Mine D has mineralization that is typically located along high angle faults, dykes, certain strata and in quartz stockworks, which has been caused by a Jurassic age intrusion. The data were collected from these geologically and geographically diverse locations, providing a suitable dataset to ensure the methods presented in this study can work in different settings.

First, this study presents the methods used to create flight plans for collecting photogrammetric data. Then, the UAV-based blasting process monitoring was conducted in three different stages, including pre-blast, blast and post-blast. In the pre- and post-blast stages, the collected aerial data were used to create 3D point cloud models and orthophotos for analysis. These models enabled the determination of the quality of blasting and assessing blast-induced damage on the final pit walls. The pre- and post-blast terrain models were used to estimate the volume expansion (rock swell) and broken rock pile (muck pile) movement. For the blast monitoring stage, a high-speed camera mounted on a UAV was used to diagnose a blast.

2. UAV Flight Plans for Collecting Photogrammetry Data

In this study, two UAV platforms were used to collect data during the field experiments. The DJI Matrice 600 Pro and DJI Inspire 2 were used for data acquisition. The DJI Matrice 600 Pro hexa-copter was selected for its high payload capacity, the versatility of its payload configurations (which include a high-speed camera setup) and for its redundant control system. The high-speed camera setup required the installation of an onboard computer to trigger the camera using the UAV remote controller and an first-person view (FPV) camera for visual feedback during flight. The DJI Inspire 2 was used because it is simpler to operate and easier to transport. However, the DJI Inspire 2 is limited to a single camera setup. The cameras used for the digital photogrammetry were the DJI Zenmuse X5 and X5S with a DJI 15 mm f/1.7 ASPH lens and an Olympus M.Zuiko 45 mm f/1.8 lens. The DJI Zenmuse X5 and X5S are 16 megapixel (MP) and 20.8 MP cameras, respectively. At the start of each flight, camera settings and exposure value were chosen and then locked using the camera's built-in auto exposure function. The UAV platforms have a stabilized camera with camera orientation control. For highwall mapping, the camera was aligned with the horizon, facing the wall. For bench, drillhole and muck pile surveying, the camera was tilted down to the nadir. Furthermore, the GPS time synchronization between the UAVs and their cameras produced georeferenced images, which enabled analysis of the generated 3D point clouds. UAV, camera, lens selection and camera settings are provided for each UAV survey in Appendix A.

When using an UAV system to collect photogrammetric datasets, the quality of the data collected depends on several parameters, including overlap between photos, distance from the target, lighting and weather conditions, focal length of the lens, field of view of the lens and camera resolution. However, only limited guidelines exist for the flight planning of UAV digital photogrammetry in mining operations, which may lead to poor results if the user is not experienced with developing flight plans [14]. This is because selecting a set of flight plan parameters that are incompatible with the desired analysis can result in longer processing times, low quality or impractically large models or models with low accuracy. Therefore, understanding the relationship between the controllable flight parameters and image quality is crucial for obtaining the desired results. The distance from the target and camera orientation (i.e., tilt) are typically considered the main controllable parameters for UAV data collection.

In order to create a flight plan suitable for pit wall mapping, prior knowledge of the geology and structural complexity of the rock wall exposure is required, specifically the smallest measurable joint trace length. This knowledge is needed to determine the objective ground sampling distance (GSD). The GSD is the ground distance covered between the centres of two adjacent pixels. In this study, the desired minimum joint size varied from 0.1 m to 0.4 m for the field experiments. To achieve this precision, the target GSD varied from 0.13 cm/pixel to 2.5 cm/pixel. These results suggest that the GSD should be at least an order of magnitude smaller than the smallest joint trace length measured. Once the GSD is determined, the distance from the target, side and front spacing and flight velocity can be calculated using the following equations developed from the formulas in [20,21]:

$$z = \sqrt{\frac{\mathrm{GSD}^2 i_w i_h}{4 \tan\left(\frac{f_h}{2}\right) \tan\left(\frac{f_v}{2}\right)}} \quad (1)$$

$$s = 2z \tan\left(\frac{f_h}{2}\right)(1 - \text{overlap}_{\text{side}}) \quad (2)$$

$$f = 2z \tan\left(\frac{f_v}{2}\right)(1 - \text{overlap}_{\text{front}}) \quad (3)$$

$$v_f = \frac{s}{t_p} \quad (4)$$

where i_w is the camera's image width, i_h is the camera's image height, f_h and f_v are the lens horizontal and vertical angle of view, z is the distance from the target, s is the side spacing between pictures, f is the front spacing between pictures, v_f is the flight velocity and t_p is the time between taking pictures (shutter interval). Target distance, camera tilt, front overlap, side overlap, flight speed and GSD (i.e., model resolution) are provided for each UAV survey in Appendix A.

To obtain the distance from the target, z, from Equation (1), the required GSD is chosen based on the target area being measured considering the joint size or the type of analysis to be conducted. With the distance from the target, the side and front spacing are calculated using the target side and front overlap using Equations (2) and (3). The flights for highwall mapping are best executed when the drone flies in a horizontal line parallel to the wall of interest with the camera directed horizontally towards the wall. This is because the flight elevation is only set once for the complete horizontal flight line. During highwall mapping, the distance between the horizontal flight lines (front spacing) and between images on the horizontal lines (side spacing) is reduced to increase overlap, while the distance from the face remains constant. Figure 1a shows a schematic of the overlaps; the front spacing is the distance between the two blue lines. The overlap that was used for highwall mapping at Mine A was 90% front and 70% side overlap. In Mines B, C and D, photogrammetry data were collected using an 80% front and 80% side overlap. Both cases were within the recommended range for digital photogrammetry [13,14,22]. Equation (4) is used to estimate the maximum lateral speed of the flight to ensure the correct side overlap of images. Typically, the slowest possible flight speed is desired to minimize the blur in the captured images. Often, the shutter speed is controlled by the camera used; therefore, the speed of the vehicle needs to be adjusted accordingly. However, if the speed is too low, it increases the flight time and battery power requirements, which might have an impact on the success of the field data collection campaign.

Once all the flight parameters are calculated, the digital elevation model (DEM) of the area of interest is used to create contour lines in QGIS, an open source GIS software [23]. The contour lines are spaced vertically such that the front overlap is achieved using the contour spacing when the camera is directed towards the wall. These lines are trimmed and simplified to ensure a more efficient flight. Subsequently, the contours are offset horizontally away from the wall by the distance from the target to create highwall mapping flight paths. Figure 1b shows an example of the flight paths used, in magenta, for Mine D. In this case, a total of 20 horizontal flight lines were used to cover a pit wall of 28,420 m^2 with a total flight distance of 6831 m. The flight plan design in Figure 1b shows the area of interest outlined in red and the DEM created for the area to provide contours. This DEM was contoured at the appropriate interval using the front spacing obtained from Equation (3). The contour geometry was then simplified to ensure smoother UAV operations and reduced flight times.

For mapping a blasted muck pile or a blast location, the distance from the target is determined from Equation (1). The target distance (flight height) and desired overlap, along with a polygon of the area of interest, can be used as input to generate a flight plan automatically using the DJI Ground Station Pro application. The area surveyed, flight time and number of images collected are provided for each UAV survey in Appendix A.

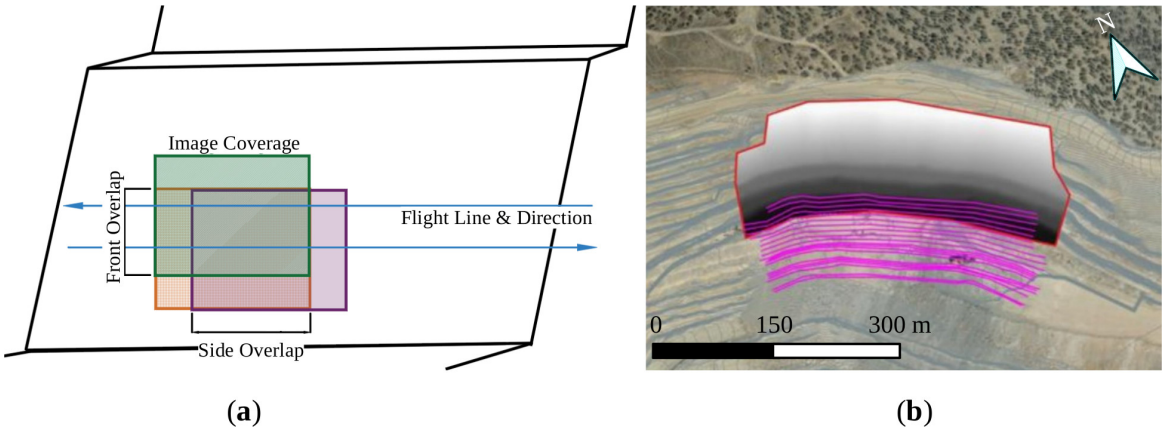

(**a**) (**b**)

Figure 1. (**a**) Schematic of the overlap and flight path design for pit wall mapping. (**b**) Flight plan design for Mine D; the flight paths are shown in magenta, and the area of interest is outlined in red with the DEM inside the outline.

Once the images were collected and sorted, they were processed in either OpenDroneMap (ODM) [24] or Agisoft Metashape [25], digital photogrammetry software to generate 3D coloured point clouds, orthophotos and DEMs. These models were used to evaluate the quality of the blasting practices depending on the type of analysis conducted. Appendix A provides the type of model constructed from each UAV survey and the section(s) analysed within the study. Software choice was based on availability and capability. OpenDroneMap was used for smaller area models and in Mines A and B for highwall mapping because Agisoft Metashape was unavailable. For Mine C and D highwall mapping, Agisoft Metashape was used for its capability to construct large high-quality models. Most surveys used high-resolution and high-quality settings to construct models. Default settings were used for muck pile and drillhole surveys because the model quality was sufficient for the analysis conducted. Coloured point clouds, orthophotos and DEMs were built in the digital photogrammetry software, and no additional post-processing was applied before analysis, except ground control point (GCP) georeferencing. Digital photogrammetry software and settings for each UAV survey are provided in Appendix A.

The image georeference accuracy is critical for the point cloud reconstruction. If a cloud is incorrectly oriented or in the wrong location, the use of the 3D point cloud may result in erroneous analyses; however, if the relative accuracy is high, it can still be used for structural mapping [26]. The images captured using the UAV systems are georeferenced using the onboard GPS; however, it is difficult to obtain reliable positional data in the air. Conventionally, ground control points (GCPs) can be used during data collection to address this issue. The GCPs are points of known locations that can be identified in the captured images. Using GCPs can improve the accuracy of the point clouds and can be used to quantify the error. It is particularly difficult to set up GCPs on a pit slope as there is usually no access to the target areas. Pit wall prisms along the benches can be used as GCPs if they are clearly visible. All pit wall reconstructions were compared to known measured points to determine whether they were suitable for analysis use because no GCPs were visible in the survey area.

The georeferencing method and the amount of GCPs used for each UAV survey are provided in Appendix A. When georeferencing using GCPs, an initial model was built using the exchangeable image file format (EXIF) data stored in the images. This initial model was then georeferenced with GCPs using the Poly 1 method in the QGIS georeferencer plugin. The Poly 1 method was used because of the low number of GCPs available in each survey area.

3. Pre-Blast Monitoring

From a blasting perspective, an accurate mapping of the bench area to be blasted is critical for a precise blast pattern design and implementation. A detailed survey of the blast location and bench wall allows for quality control of drillhole alignment and pattern implementation. Moreover, it allows

for calculation of the in situ volume of the rock mass in the blast location and a better understanding of the structural characteristics of the rock mass. The following section will describe the application of UAV technology for pre-blast monitoring.

3.1. Structural Mapping

One of the key advantages of digital photogrammetry is that once a 3D point cloud of the pit wall is generated, it is possible to both conduct virtual structural mapping and assess the blast induced damage of the pit wall on the same point cloud model. Structural mapping of the pit wall is important for both geomechanical stability analysis of pit slope and estimating the IBSD. The IBSD is defined by the intersection of naturally occurring joints within the rock mass [27]. These joints are defined by their orientation, persistence, frequency and surface geometry [28]. However, defining these characteristics can be challenging due to their three-dimensional nature and the field exposure of joints, which generally provides only two-dimensional information [29]. Further to this limitation, exposures are often inaccessible for the manual mapping of joint characteristics. This is particularly true in the case of open pit mines, where once the benches are fully excavated, access to these benches becomes difficult or hazardous for personnel.

Through the use of UAV technology, it is possible to collect 2D images of the pit wall to generate a 3D model or an orthophoto for structural mapping and assessing the impact of blasting on the final wall geometry. By using virtual mapping, it is possible to accurately measure the orientation and trace length of joints exposed on the pit wall. The use of a UAV allows coverage of a large area, typically inaccessible for conventional structural mapping, such as window mapping, which involves having a person conduct mapping on or close to the rock face in a window with fixed height and width [8]. It also generates a more extensive, high-resolution structural dataset. A statistical analysis of data can be used to generate a stochastic model of jointed rock mass based on a 3D discrete fracture network (DFN). A DFN is a stochastic model of the fractures within a rock mass, which can be used to estimate the IBSD required for the blast analysis [30]. The accuracy and reliability of the DFN model is dependent on the quality of the mapping data collected [31]. Therefore, the UAV's ability to collect more data at a high resolution should produce more robust DFN models. Structural mappings were conducted at Mines A-D using the A1, B1, C1, and D1 UAV surveys, detailed in Appendix A.

Using UAV and digital photogrammetry methods, the pit wall mapping time can be significantly reduced compared to manual mapping methods. At Mine D, a mapping-rate of approximately 44.6 m^2/h was achieved using conventional window mapping in cells of 1.8 m high by 19.2 m long. On average, only 20 of these windows can be mapped during a shift by appropriately trained personnel. Through the use of a UAV, a mapping-rate of 490 m^2/h was achieved, which is more than ten times faster than manual mapping. The images collected also provide a permanent record of the rock mass at a certain time, allowing site personnel to quantify any changes in the rock over time. It also becomes possible to collect and map data that were previously inaccessible, in addition to collecting data for a much larger area. The area used for mapping, the time required for virtual mapping, the estimated field mapping time based on the 44.6 m^2/h rate and the virtual mapping method used for different mine locations are described in Table 1. The methods and speed of mapping are described further below. Using UAV systems for data collection will not eliminate field observations, as the collected data need to be verified through ground sampling, and joint surface information cannot yet be accurately collected using UAV systems, which is required for rock mass rating systems [8].

The joint mapping was done using the 3D point clouds directly in CloudCompare [32], an open source software. Using this software, it was possible to measure the joint dip, dip direction and length of traces—all required to define joint sets and to estimate the IBSD of rock mass. The Compass tool by Thiele [33] was used for manual and semi-automated structural mapping on the cloud using the default "Darkness" trace mode, while the Facets tool developed by Dewez [34] was used for automated joint identification using default settings. Automated joint detection algorithms were run for all sites, with differing degrees of success. The automated option creates facets on the exposed joint surfaces

and is useful where joint surfaces are clearly exposed on the pit wall. For highly irregular jointing or low-quality point cloud models, manual or semi-automated mapping should be used. Using manual virtual mapping can significantly increase the time required to complete the mapping of the wall. For example, for Mine B, the automated joint identification was significantly faster; 3D model creation, joint identification and analysis took only 5 h compared to 24 h for manual virtual mapping of the same wall.

Table 1. Summary of the mapping area, virtual mapping method and mapping time (virtual and field mapping) used for each mine.

Location	Area (m^2)	Virtual Mapping Method	Virtual Mapping (h)	Estimated Manual Field Mapping (h)
Mine A	3170	Manual	79.5	71.1
Mine B	5210	Automated	5	116.8
Mine C	3510	Semi-Automated	36	78.7
Mine D	28,420	Semi-Automated	58	637.2

The automated and manual mapping in Mine B had similar orientation results (see Table 2). It should be noted that the trace lengths were only similar for Set 2, while Sets 1 and 3 had different mean trace lengths for the two mapping methods. The trace lengths were measured as the longest dimension of the facet when using the automatic mapping method. The difference in trace length was caused by facets splitting slightly offset joints in close spatial proximity into multiple components. In manual mapping, the same joints were mapped as a single joint. This resulted in longer trace lengths during manual mapping than automated mapping. The overall areal fracture intensity (P_{21}) was similar for both manual and automated mapping, indicating that the total length of joints for each set was similar. However, the automated mapping still required manual post-processing to identify the joint sets and calculate the average trace lengths. This method was unable to detect the horizontal bedding, which was exposed as traces on the surface of the rock mass.

Table 2. Comparison of automated and manual virtual mapping results for Mine B.

Set	Automated				Manual			
	Dip (°)	Dip Direction (°)	Mean Length (m)	P_{21} (m^{-1})	Dip (°)	Dip Direction (°)	Mean Length (m)	P_{21} (m^{-1})
1	71	160	5.5	0.13	69	160	6.7	0.15
2	78	81	3.0	0.05	78	87	3.2	0.06
3	80	273	2.0	0.03	83	265	3.9	0.03
4	–	–	–	–	0	NA	22	0.09

At Mine A, mapping was done with fully manual methods because of the lower quality of the point cloud. Using this approach involved manually tracing the length of the joint and visually fitting a plane in CloudCompare to estimate the dip and dip direction of the joint. To fit a new 3D plane in CloudCompare, the dip and dip direction were iteratively changed until the inserted plane visually fit the joint. This highly manual approach resulted in a very slow mapping rate. The flight plan at Mine A had a lower side overlap, which produced the lower quality point cloud during ODM's dense cloud construction. To mitigate this at Mines B, C and D, a front and side overlap of 80% was used. Mine B had three well-defined and exposed joint sets, which made it suitable for automated joint identification, and therefore very fast for mapping. At Mines C and D, there were no clearly exposed joint surfaces, and the automated detection method could not be used. However, the semi-automated method could be used because the point clouds were sufficiently high quality; this method traces the selected joint and then estimates its length, dip and dip direction. This approach is faster than the manual method and field mapping. The difference in time requirement can be seen in Table 1.

Figure 2 shows example windows of pit wall mapping for Mines A, B and C to illustrate the structural variability between sites, the joint trace and joint plane measurements captured and point cloud quality. With the joint trace length information and the area of the digital photogrammetric

model, it is possible to calculate the areal fracture intensity (P_{21}) of the mapped pit walls; a key input for the development of a DFN model [35].

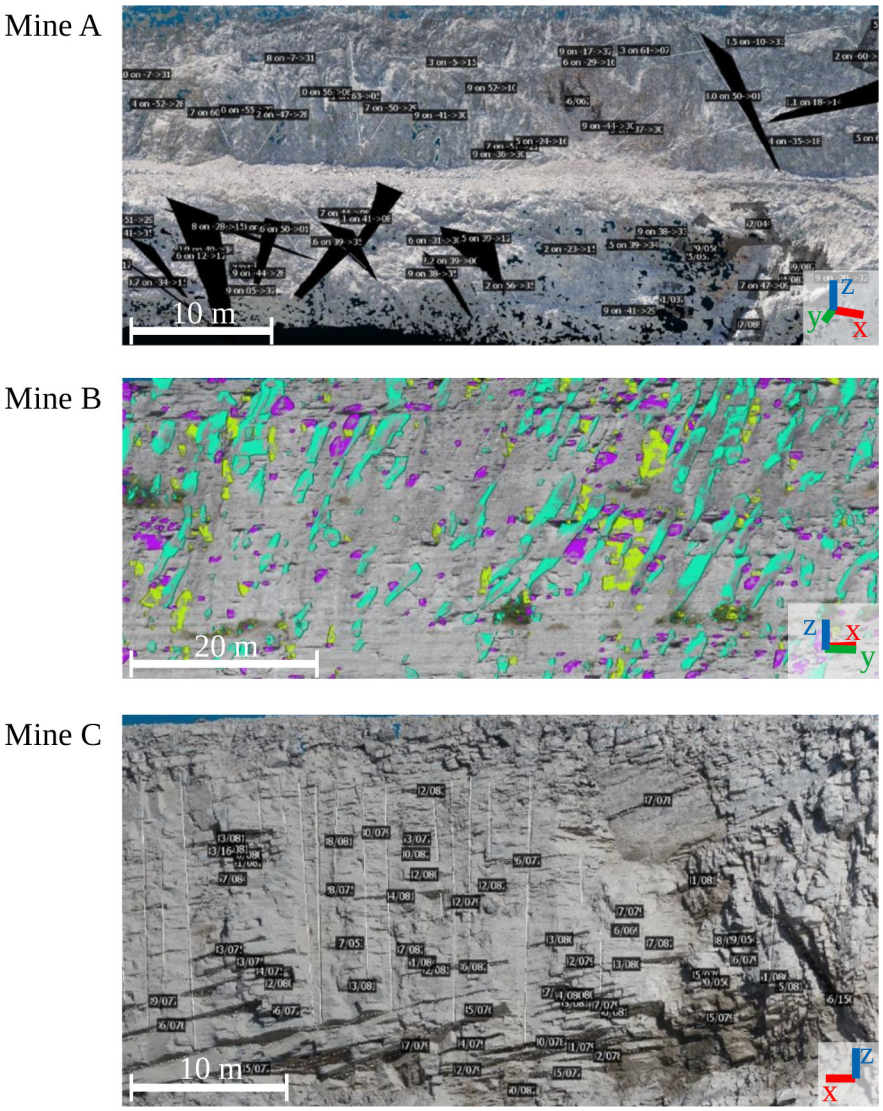

Figure 2. Example of pit wall mapping using a UAV for Mine A (manual virtual mapping), Mine B (automated virtual mapping) and Mine C (semi-automated virtual mapping).

Figure 3 shows an example of the areal fracture intensity (P_{21} in m/m^2) of two benches mapped at Mine D. Figure 3a shows the point cloud of the two benches that were mapped in CloudCompare using the Compass tool. The joint lengths were recorded and subsequently used to visualize the P_{21} in CloudCompare. The major structure is highlighted by the dashed black lines. The "Estimate P_{21} intensity" function with the Compass tool was used to visualize the P_{21} by using the measured joint lengths and dividing them by the point cloud area. During virtual mapping, an attempt was made to exclusively map natural fractures (i.e., joints) for the estimate of P_{21}. This ensures that the P_{21} estimated represents in situ conditions. Other fractures on the wall include blast-induced fractures, which do not occur naturally and are only found in the rock mass local to blasting activity. The area of the bench was estimated in this study by cutting sections in 5 m intervals and measuring the heights over the length of the pit wall. The area of the bench can also be calculated using the 3D mesh, but in this study, we used 2D sections. Figure 3b shows the P_{21} values on the two mapped benches with the same major structure highlighted as in Figure 3a. The figure demonstrates the spatial variation of P_{21} on the pit walls, with the highest P_{21} intensity on the middle of the lower bench around a local

structure. Using this tool, it is possible to identify areas with high fracture intensities and areas of potential IBSD variation through visualization.

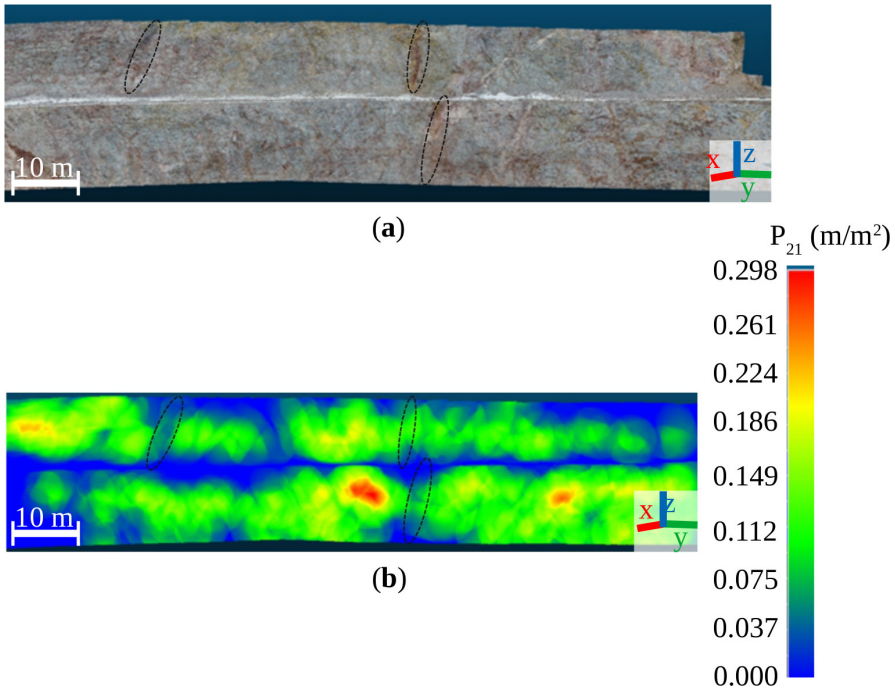

Figure 3. (**a**) Section of Mine D pit mapped (two benches). (**b**) P_{21} fracture intensity mapped on the pit wall (red represents higher fracture intensity zones, and blue represent lower fracture intensity areas).

In this study, DFN models were developed for Mines A and B using data acquired from drone-based pit wall mapping. A DFN model stochastically describes the geometrical characteristics of rock mass fractures or, in general, discontinuities [36]. The basic objective of DFN modelling is the generation of simulated fractures that accurately represent the salient characteristics of a population of fractures sampled in a particular rock mass. The fundamentals of discrete fracture network (DFN) modelling were explained by Dershowitz [37]. DFN modelling has been used in a variety of mining applications, including dilution estimation [38], caving fragmentation analysis [39], estimation of rock mass strength [40,41], stability analysis of surface and underground excavations [40,42] and blast parameter assessment [43,44].

Joint sets are defined by their orientation, size, frequency and surface geometry. The availability of a high-quality 3D point cloud ensures the collection of accurate joint parameters, which leads to increased reliability of 3D DFN models [45]. Once the joint sets were identified, it was possible to estimate a statistical distribution of their orientations and trace lengths. Furthermore, by using the total trace length of each set, the areal fracture intensity (P_{21}) was estimated for the whole mapped area. In this study, the DFN generation was carried out using an iterative process in FracMan [46], a discrete fracture network (DFN) modelling software, where an arbitrary volumetric fracture intensity (P_{32}) (the area of fractures within a certain volume) was assigned to each joint set. The P_{32} can be inferred from the P_{21} since it cannot be directly measured in the field [47]. A trace-plane or survey surface of mapped location was inserted into the DFN model, and the orientations and trace lengths of joints were recorded on the surface. The results were compared to the virtual structural mapping data measured using the UAV photogrammetric model. The P_{32} of the individual sets were adjusted after each simulation until there was good agreement between the P_{21} of the virtual structural mapping data and DFN model (Tables 3 and 4), resulting in a model that was acceptable for use in IBSD estimation. A low P_{21} percent error was considered as acceptable agreement for this study. The spatial variability within the rock mass for the individual joint sets was not considered; the rock mass was modelled using the average P_{21} of each set. Similarly, the length of the joint sets was adjusted until the trace

length of joint sets produced in the DFN matched the virtual structural mapping data (Tables 3 and 4). Figure 4 presents the 2D traces of the DFN models developed for Mine A and Mine B and the 2D trace-planes of the same pit walls that were virtually mapped.

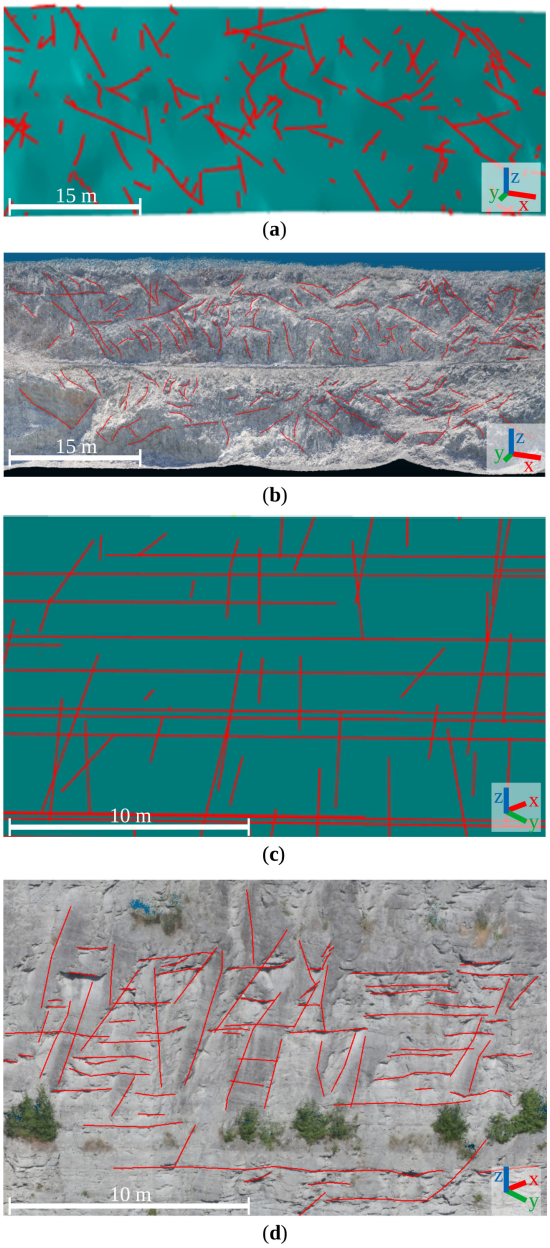

Figure 4. Trace-planes of DFN models (green) generated for (**a**) Mine A and (**c**) Mine B. Red lines represent joint traces. Trace-planes of UAV virtual mapping generated for (**b**) Mine A and (**d**) Mine B.

Tables 3 and 4 show the distribution of DFN input data used for the joint sets and the resulting DFN mean trace lengths and P_{21}; these results are also compared to the virtual structural mapping data for Mines A and B, respectively. The results demonstrate a good agreement between virtual mapping data and DFN models. It took over twenty DFN generations of Mine A to calibrate the model, compared to nine for that of Mine B. This difference in the number of DFN generations reflects the additional structural complexity of the rock mass at Mine A. Figure 5 shows examples of stereonet agreement between field data and DFN model data for Mine A and Mine B. The bedding planes at Mine B visible in Figure 4d were deterministically modelled in the DFN because they were horizontal with no variation in dip.

Table 3. Comparison of Mine A virtual mapping data and DFN model data.

Set	Dip (°)	Dip Direction (°)	DFN Model Inputs			DFN Model Outputs		Virtual Mapping	
			Distribution	Mean Size (m)	StDev (m)	P_{32} (m^{-1})	Mean Length (m)	P_{21} (m^{-1})	Mean Length (m)	P_{21} (m^{-1})
1	45	356	Log-normal	1.17	0.78	0.14	4.2	0.08	4.4	0.08
2	85	345	Log-normal	0.70	0.33	0.06	2.0	0.01	2.1	0.01
3	78	104	Log-normal	0.75	0.65	0.21	2.4	0.10	2.6	0.09
4	89	60	Gamma	1.96	0.49	0.09	4.0	0.07	4.0	0.07

Table 4. Comparison of Mine B virtual mapping data and DFN model data.

Set	Dip (°)	Dip Direction (°)	DFN Model Inputs			DFN Model Outputs		Virtual Mapping	
			Distribution	Mean Size (m)	StDev (m)	P_{32} (m^{-1})	Mean Length (m)	P_{21} (m^{-1})	Mean Length (m)	P_{21} (m^{-1})
1	71	160	Gamma	2.13	0.39	0.35	5.8	0.16	5.5	0.13
2	78	81	Log-normal	0.89	0.62	0.10	2.9	0.04	3.0	0.04
3	80	273	Log-normal	0.57	0.49	0.12	1.9	0.03	2.0	0.03

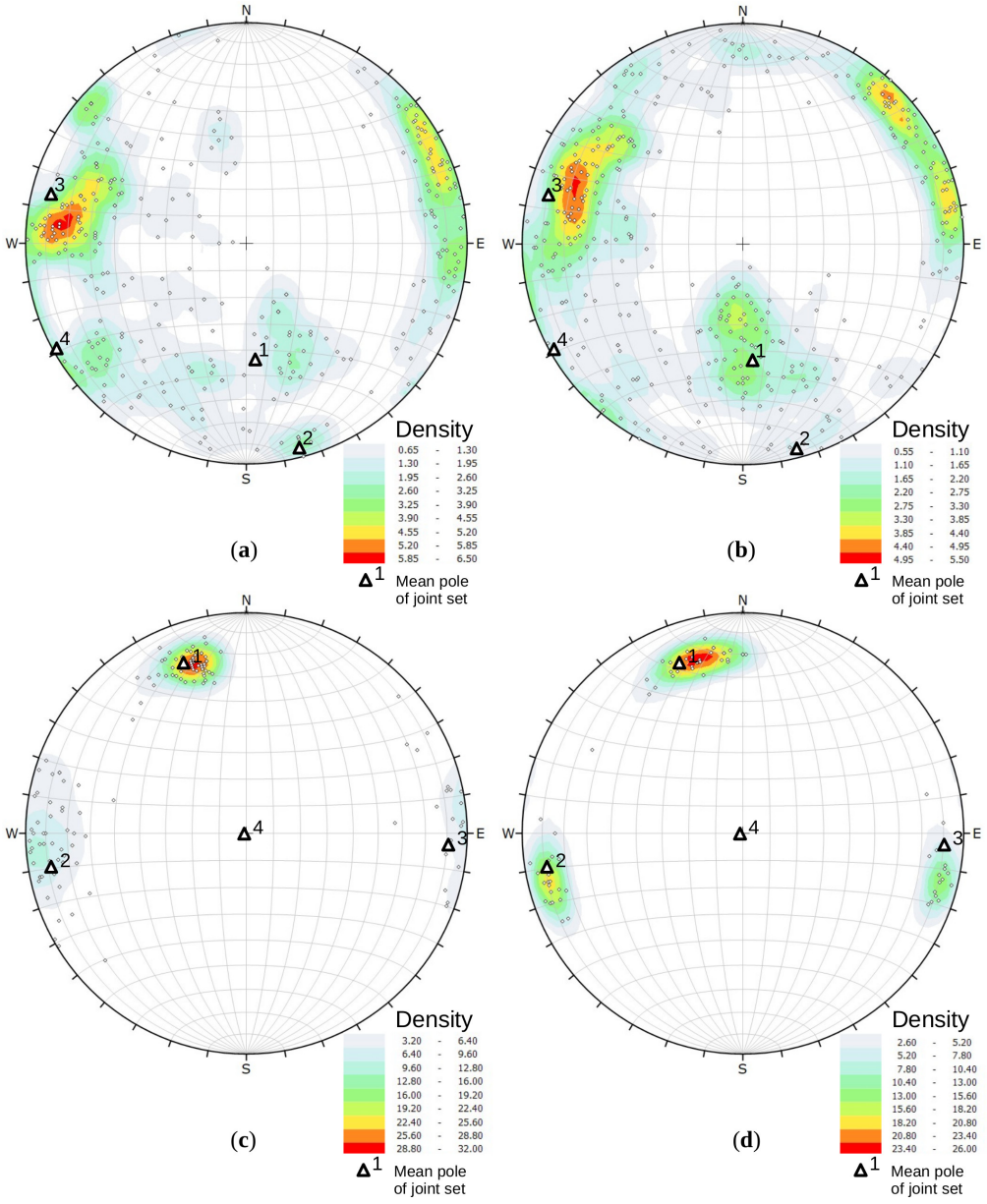

Figure 5. Mine A lower hemisphere equal area stereonets with (**a**) virtual mapping data (311 pole vectors) and (**b**) the DFN model (361 pole vectors). Mine B lower hemisphere equal area stereonets with (**c**) virtual mapping data (132 pole vectors) and (**d**) the DFN model (75 pole vectors). The bedding planes at Mine B were not included in the stereonets because they would only appear as a point with high concentration. Mean poles of joint sets described in Tables 3 and 4 are labelled as triangles in the stereonets.

3.2. IBSD Estimation

Once the DFN models were determined to be suitable representations of the rock mass at Mine A and Mine B, a deterministic estimation of IBSD was conducted using the ray cast volume method [46]. It is recognized that in a comprehensive analysis, more realizations of the DFN model should be undertaken in order to determine the possible variation of IBSD estimation. For example, fifty simulations were used by Elmo et al. [35] to provide an estimate of unstable block volumes. The ray cast volume method is based on a simple algorithm for calculating block size; the algorithm generates random points within the DFN model that are used as origins of rays, which are cast outwards until the rays intercept a fracture. The length of these rays is sampled a defined number of times, and the mean length is then used to estimate the volume of the blocks. IBSD estimation

was conducted for Mines A and B using the A1 and B1 UAV surveys described in Appendix A. The IBSD results for Mines A and B are plotted in Figure 6 (the solid red and blue lines). The results show that the median in situ block sizes in Mine A and Mine B are 14 m and 4.7 m, respectively. The same figure shows the blasted block size distribution (BBSD) for Mines A and B, which will be discussed in Section 5.1.

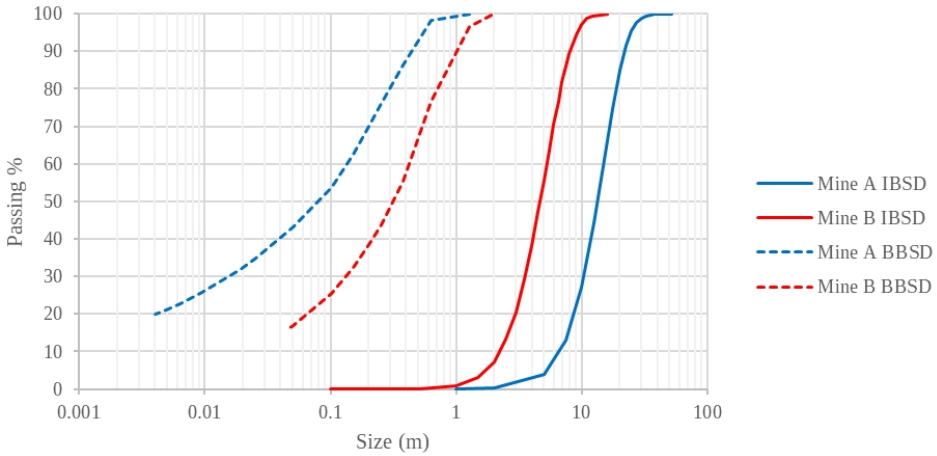

Figure 6. Particle size distribution plots for Mines A and B. The IBSDs estimated using DFN models are illustrated with solid lines. The BBSDs measured using image analysis for Mines A and B are drawn using dashed lines. BBSD measurement is described in Section 5.1.

3.3. Assessment of Drillhole Alignment

Accurate implementation of a blasting pattern in an open pit mine can improve the result of rock fragmentation and reduce the drawback of the blasting processes. Blasthole deviation is frequently experienced in open pit mines. The consequences of blasthole deviation include build-ups, hang-ups and poor rock fragmentation and normally lead to extra drilling, loss of drill rods, ore dilution, ore loss, increased explosive consumption, time wastage and delays in the production operations. The deviation of blastholes is usually divided into four different classes, including collaring deviation, alignment deviation (horizontal direction and vertical inclination), drilling deflection and depth. According to [48], a blasting operation will not be effective if the blastholes are poorly placed or aligned. The deviation of blastholes will increase the excessive burden or reduce burden, which will lead to an undesirable fragmentation size distribution. Studies have shown that if a hole is misplaced by 0.4 m, it could reduce the explosive power at a certain point by about 28% [48]. Moreover, the same authors showed that the cost of drilling and blasting can increase as collar hole deviation increases.

Drillhole alignment assessment was performed for a blasting pattern of 230 holes with a diameter of 225 mm at Mine D. The designed blasting pattern was staked out for drilling equipment using ground-based surveying. The UAV survey was done with the DJI Inspire 2 drone at a GSD of 1.13 cm/pixel. Details of the UAV survey used for this experiment are provided as D2 in Appendix A. The orthomosaic of the blast location was built in digital photogrammetry software and georeferenced using the GCPs in the area and the georeferencer plugin in QGIS. GCPs were required for this analysis because the model should have an error that is much lower than the desired maximum hole deviation at the mine. The aerial mapping of the blast location can also be used for the development of a pre-blast DEM that can then be used for estimation of blast-induced volume expansion (swell). Once the orthomosaic was georeferenced, the centre of visible blastholes was annotated to survey the actual pattern. Then, the designed blasting pattern was superimposed for comparison. The deviation in the collar location was calculated for each blast hole by computing a distance matrix in QGIS between the actual pattern and the designed blasting pattern. It should be noted that the depth deviation cannot be assessed with this method.

Figure 7 shows the results of the UAV survey conducted in Mine D to assess blasthole alignment. Figure 7a shows the orthomosaic with the designed blasting pattern (blue) and actual pattern (gradient red). Figure 7b presents the histogram of the blasthole collar deviation for the implemented pattern. The desired maximum deviation at Mine D was 0.3 m (1′). The measured maximum deviation was about 3.6 m (12′). Large collar deviation was observed for the first row of holes, near the free face, and for the pre-split and buffer holes. The results indicate the importance of a detailed survey of a blast location prior to blast pattern design. It is evident that some of the blast holes drilled very close to the bench crest could have been eliminated from the blast pattern design, thus reducing the total drilling cost and time. Due to the deviation in control and buffer holes, there may be an increase in blast-induced pit wall damage and an increase in underbreak and overbreak. These effects may result in pit wall instability and/or economic impact. More discussion about the effect of pre-split hole deviation and quality control during post-blast monitoring is provided in Section 5.3.

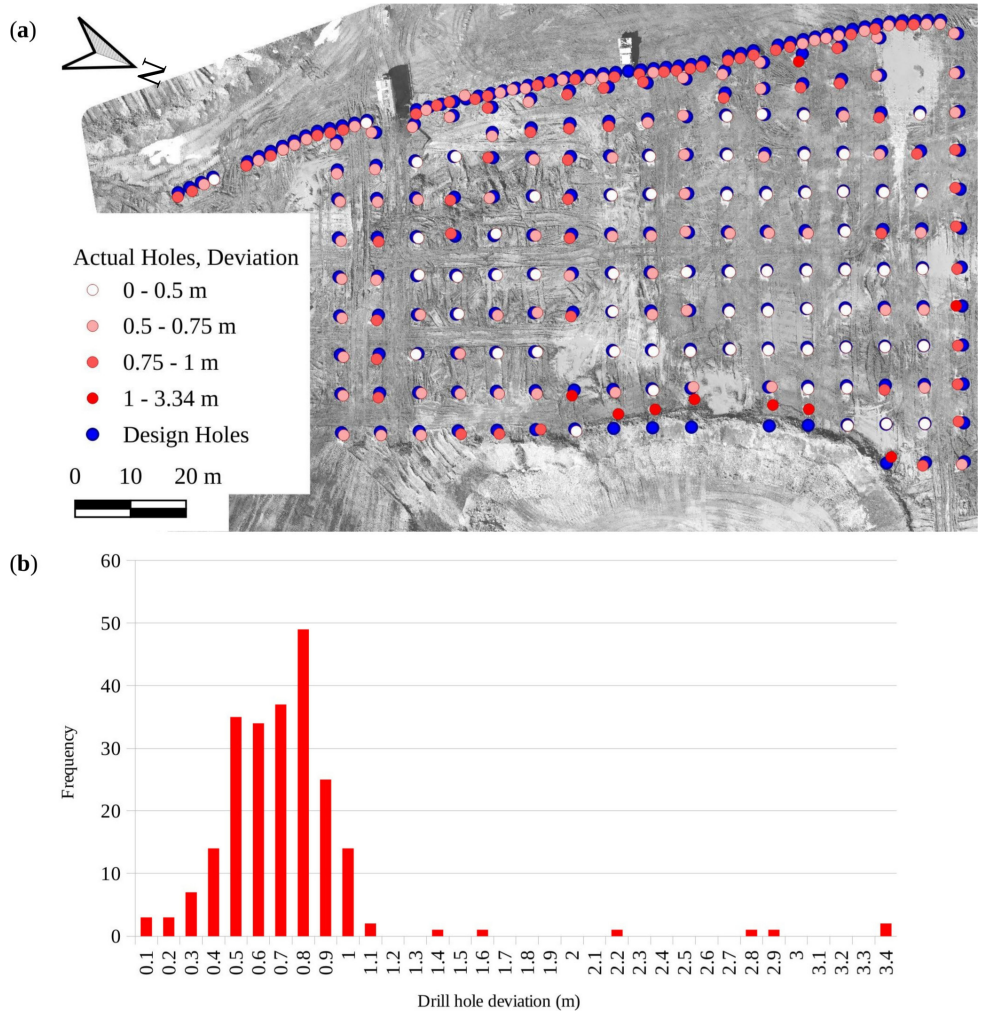

Figure 7. Blasthole deviation analysis for 230 holes with a diameter of 225 mm at the blast location in Mine D. (**a**) Orthomosaic with the designed (blue) and implemented (gradient red) blast pattern. (**b**) Histogram of visible drill hole collar deviation for the implemented blast pattern.

4. Blast Monitoring

4.1. Monitoring Blast Dynamics Using a High-Speed Camera

It is possible to use high-speed cameras to capture images of mine blasts in order to identify areas with poor performance, such as stemming ejection and gas loss through the face and fly rock. Moreover, the high-speed camera can be used to estimate the face velocity, trajectory and burden displacement [7].

However, with ground-based high-speed camera monitoring, there are a few limitations, including reduced image clarity due to dust and fumes from the first row of blast holes and possible occlusions resulting from poor viewing locations [7]. Recent advances in low-cost, easy-to-use and lightweight high-speed cameras make them available for use on UAV systems. The aerial method allows for an appropriate camera placement with respect to the blasting sequence, which is crucial for generating high-quality images. To date, the aerial method has not been studied for blast monitoring.

A blast at Mine D was monitored using a high-speed camera mounted on the DJI Matrice 600 Pro system. The high-speed camera used was the Slomocam Model fps4000-720C-640, which runs at 1800 fps with a 1280 × 720 resolution at that frame rate. At this resolution and frame rate, the maximum recording time of the camera is approximately one minute. Thus, the camera had to be triggered remotely using a custom-designed control system integrated with the UAV controller. This was done through the DJI Manifold onboard computer installed on the drone and powered by the DJI Ronin-MX gimbal. An FPV camera was also attached to the drone to guide video composition and identify the area of interest. The high-speed camera was triggered at a safe distance of 400 m from the blast location when the blasters started the countdown. Details of this UAV survey are provided as D3 in Appendix A. Figure 8 shows five representative frames of the blast at Mine D. Figure 8a is the time of blast initiation. The Figure 8b,c frames show stemming ejection from several blast holes. Insufficient, inconsistent or inefficient stemming allows the blast energy to prematurely vent at the collar, reducing the energy applied to breaking and moving the rock mass. Stemming ejection is a common cause of lost energy in the blast, especially when drill cuttings are used as stemming material. Figure 8d shows the moment when all holes are blasted. The last frame presented in Figure 8e is the final blast result with some minor rock falls on the nearby benches.

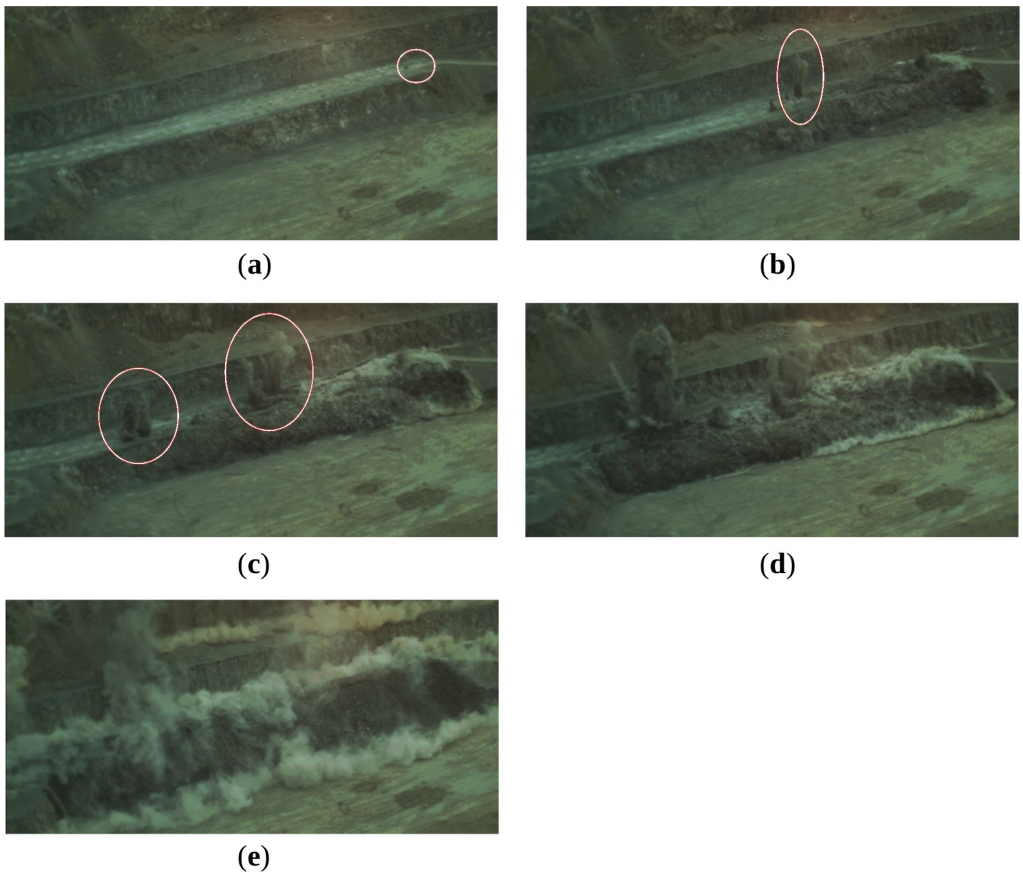

Figure 8. Frames of high-speed video footage from a blast at Mine D. (**a**) Initiation, (**b**,**c**) stemming ejection, (**d**) all holes blasted and (**e**) result of the blast.

5. Post-Blast Monitoring

5.1. Assessing Blast Fragmentation

Visual observation, sieve analysis and 2D and 3D image analysis are methods that have been used and developed to estimate the BBSD of muck piles. Image analysis methods have become more common in mining operations to estimate BBSD because they are practical, fast and provide relatively accurate measurements [49]. As discussed in detail by [12,49], image analysis techniques have several limitations, including a limit in measurement resolution and rock segmentation accuracy. Poor or incorrect rock segmentation is the most persistent limitation of image analysis method and results in the measurement of disintegrated and fused rock fragments. To mitigate this effect, extensive manual editing is usually required to correctly delineate blasted rock fragments. However, fragments are typically overlapped on the surface of the pile, which results in inaccurate measurement. Another significant limitation of image analysis is fines estimation. The image system resolution is not able to resolve to fine fragment sizes while maintaining accurate delineation, so a fines cut-off is typically applied to fragmentation measurement. Below the fines cut-off, the area of fines is commonly used to estimate fines. However, the fines on the pile surface do not represent the amounts of fines contained internally. To reduce this error, results were combined from image analysis (+10 cm) or in-pit sorting (+2.5 cm) and laboratory sieving [50]. While this improves measurement accuracy for fines, sieve sampling and in-pit sorting methods are expensive and can disrupt production. Recent 3D imaging and analysis methods have improved rock segmentation accuracy and eliminated the need for the placement of objects to set image scale and, in doing so, have reduced the errors introduced by using a uniform scale to represent an uneven muck pile surface [51,52]. While some limitations have been reduced, 3D image analysis currently requires a significant amount of capturing time for detailed scans, and when using terrestrial scanners, fixed capture locations are required to reduce smoothing 3D data.

Previous studies have shown the advantages and limitations of using UAV systems for rock fragmentation analysis [53–56]. With images collected from blasted muck piles in Mines A and B, it was possible to estimate BBSD using image analysis software. Due to the unavailability of the UAV at Mine A after blasting, it was not possible to capture an orthophoto of the muck pile. However, it was possible to collect some images of the blasted muck pile using a terrestrial camera. The terrestrial images in Mine A had an average GSD of 0.13 cm/pixel. More details of the terrestrial images are provided as A2 in Appendix A. In Mine B, the UAV with the 15 mm lens was used to collect 38 images of the blasted muck pile to generate an orthophoto with a GSD of 1.5 cm/pixel. The orthophoto is considered a better product to use in image analysis software for BBSD estimation because it is a composite of collected images corrected to have a uniform scale. This uniform scale results in a map of the muck pile without the perspective and lens distortion that might be present in a single image. The UAV survey used for fragmentation assessment is described as B2 in Appendix A. Figure 9 shows the image and orthophoto used for image analysis. In each case, the areas outside of the muck pile of interest were masked, as shown in cyan in Figure 10, to avoid including them in the analysis.

The images were then imported into Split-Desktop by Split Engineering [57] for image analysis to estimate BBSD. GSDs were used to set the image scale so that measurements can be assigned to rock fragments. The software used the input images to delineate the rock fragments using proprietary image segmentation. Extensive manual editing of the rock fragment delineation was done to improve the rock segmentation process. The final delineation network of rock fragments is overlaid on the original images in Figure 10. The fines cut-off used for the analyses were 0.39 cm and 4.5 cm for Mines A and B, respectively. This cut-off assumes that the software can measure a particle with a minimum size of 3 px. The fines cut-off is then calculated as 3 $\times$ GSD.

Figure 9. Images from Mine A (**left**) and Mine B (**right**) produced for image analysis of the blasted muck piles.

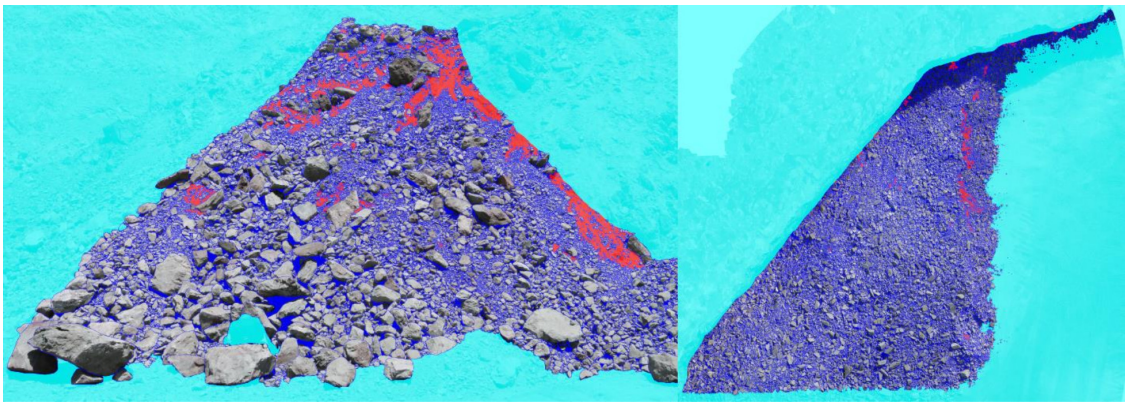

Figure 10. Rock fragment delineation for Mine A (**left**) and Mine B (**right**). Blue regions represent rock fragment boundaries; cyan regions are masked; and red regions represent fines.

Figure 6 shows the estimated BBSD produced by image analysis for Mines A and B (dashed lines). The IBSD and BBSD plots can be used to assess the viability of a mine producing the desired blasted rock size distribution and determining blast powder factor requirements [30,58,59]. Moreover, they can be used as a tool for improving the blasting process at the mines. The blast quality can be assessed by comparing the IBSD and BBSD of Mines A and B. The comparison shows that: (a) blasting causes a reduction of all the block sizes within the rock mass, with Mine A having a larger spread and size reduction; (b) the IBSD 80% passing of Mine A and Mine B was 18.7 m and 6.8 m, respectively; and (c) significantly less small fragments were generated at Mine B, with only 17% passing under 0.05 m compared to 43% at Mine A.

Various empirical relationships between the powder factor, in situ block size (IBSD) and the blasting results (BBSD) have been developed over time. The desired size fragmentation is related to the Bond work index (W_i), the in situ block size and the explosive used [58]. According to an update by Kahriman et al. [59], based on 14 case studies, the powder factor can be estimated through Equation (5).

$$q_b = 10W_i \left(\left(\frac{1}{\sqrt{D_{b80}}} \right) - \left(\frac{1}{D_{i80}} \right) \right) K \tag{5}$$

where W_i is the Bond work index calibrated, D_{b80} and D_{i80} are 80% passing for BBSD and IBSD, respectively (in micrometer) and K is a conversion constant relating the energy used in Bond's work index to the energy in ANFO and the specific gravity of the rock (ρ_r).

$$K = (860/912) \times \rho_r \tag{6}$$

where the ratio 860/912 is the amount of energy created from 1 kg ANFO in kWh (1 kWh = 860 kcal; 1 kg ANFO = 912 kcal). W_i at Mine A was 16.30, and that of Mine B was 14.95. The use of W_i introduces uncertainty in the results as W_i cannot be exactly known for each blast location. However, due to the homogeneous nature of the rock at Mine B, W_i is expected to be in a relatively narrow range. At Mine A, the confidence in W_i was lower because it was based on the initial feasibility study. Furthermore, the rock is relatively heterogeneous at Mine A.

The theoretical powder factor was calculated for Mines A and B based on Equation (5). The results presented in Table 5 demonstrate that the model results fall within the range used for blasting at Mine A. It also suggests that the current powder factor used for Mine B (which is a quarry site) is higher than the theoretical powder factor, which implies that the blasting practices at Mine B could be improved.

Table 5. Theoretical powder factor estimates, compared to the actual field values used.

Site	Theoretical Powder Factor (kg/t)	Actual Powder Factor (kg/t)	
		Average	Standard Deviation
Mine A	0.25	0.21	0.06
Mine B	0.12	0.16	0.02

5.2. Assessing Blast Impact on Final Pit Walls

The digital photogrammetry software can also be used to build a digital elevation model (DEM). The DEM can be imported into geographic information system (GIS) software to conduct an evaluation of the blast-induced damage on pit walls including bench face angles and catch bench width. In this study, QGIS [23] was used for the analysis. Figure 11 shows the DEM built for the pit wall from images collected at Mine A using the UAV survey labelled A1 in Appendix A. Figure 11b shows the actual catch bench (light blue area) and the blast-induced overbreak (light red area) overlain on a raster representing the slope. The results of the catch bench width measurement analysis are presented in Figure 12. The histogram was created by estimating the catch bench width between the toe and crest location along the slope model using sections. To estimate the catch bench width, the toe and crest were traced in QGIS, and then, these lines were used to create endpoints for sections at 0.5 m intervals. The interval between section endpoints was assumed to be large enough for a bench width analysis based on the 20 m double bench height. The distance between matching points along the toe and crest can be calculated through computing a distance matrix in GQIS and then used for a statistical analysis of the catch bench width. Moreover, the area of catch bench loss can be estimated by comparing the location of the planned crest to the actual location on the raster representing the slope. As can be seen in Figure 11b, significant catch bench loss occurred at Mine A, where in this area, 51% of the designed catch bench was lost. Some areas had significant back break, which can compromise the safety of workers and equipment in lower benches as an insufficient bench width is maintained to catch any falling material. The blasting and wall control practices in this particular area were inadequate for maintaining the required catch bench.

Through the use of the generated point cloud, it is possible to compare the as-built versus designed bench face angles. Using CloudCompare, the normal vectors of the surface of points within the point cloud were computed using a search radius of 1.57 m. The search radius chosen automatically in CloudCompare using the point cloud octree was considered appropriate based on the large size of the analysis area. Then, the point normals were re-oriented by starting at a random point and propagating the normal orientation to its neighbours. This can be done either using a fast-marching method, which calculates the normal orientations on a grid, or using a spanning tree based on a maximum number of neighbours [32]. The results will vary based on the method and settings used. The default setting of six nearest neighbours on the minimum spanning tree, using the fast-marching method, was used in CloudCompare to estimate the point cloud normal orientations. Once the normal orientations are estimated, the difference between the normal vectors and the target bench face angle are calculated by adding a constant scalar field. In high density point clouds, the high number of points can make it

difficult to interpret results at a large scale. To address this issue, the points can be clustered further to downsample the cloud and produce clearer results that are easier to interpret, but this also reduces the variation in the slope angle. The clustering radius can depend on the scale of the analysis and the ease of result interpretation.

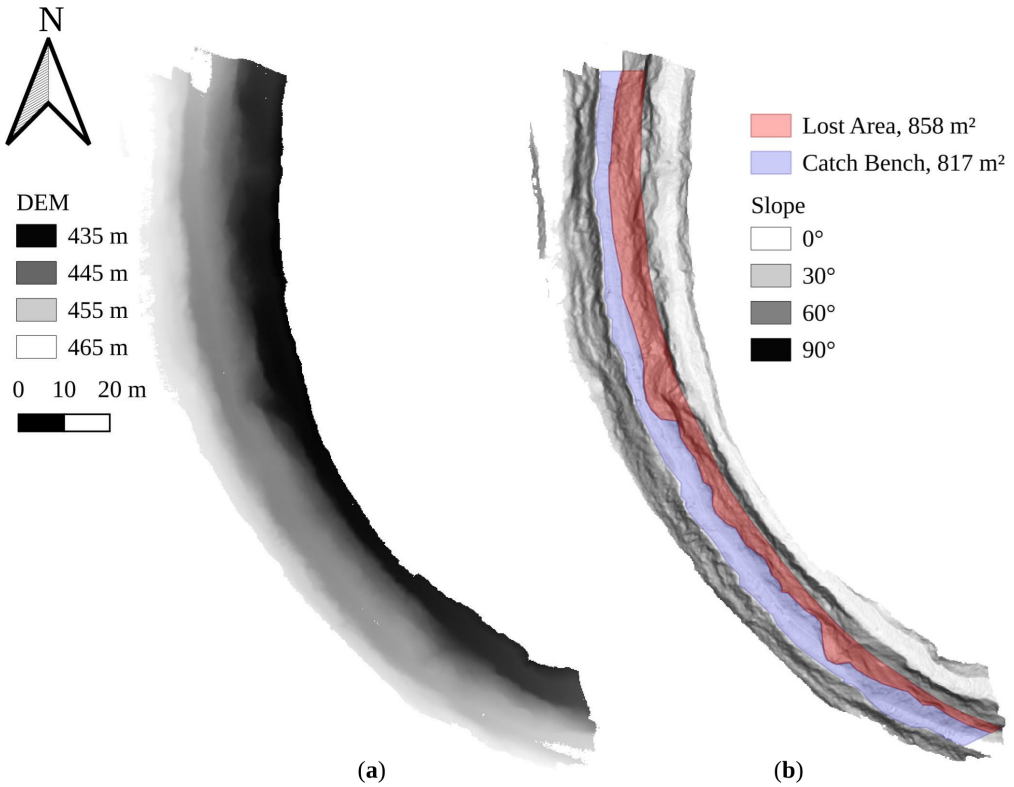

Figure 11. (**a**) DEM of Mine A. (**b**) Raster representing the slope used for bench width analysis. The actual catch bench area is shown in light blue, and the blast-induced overbreak causing lost area is shown in light red.

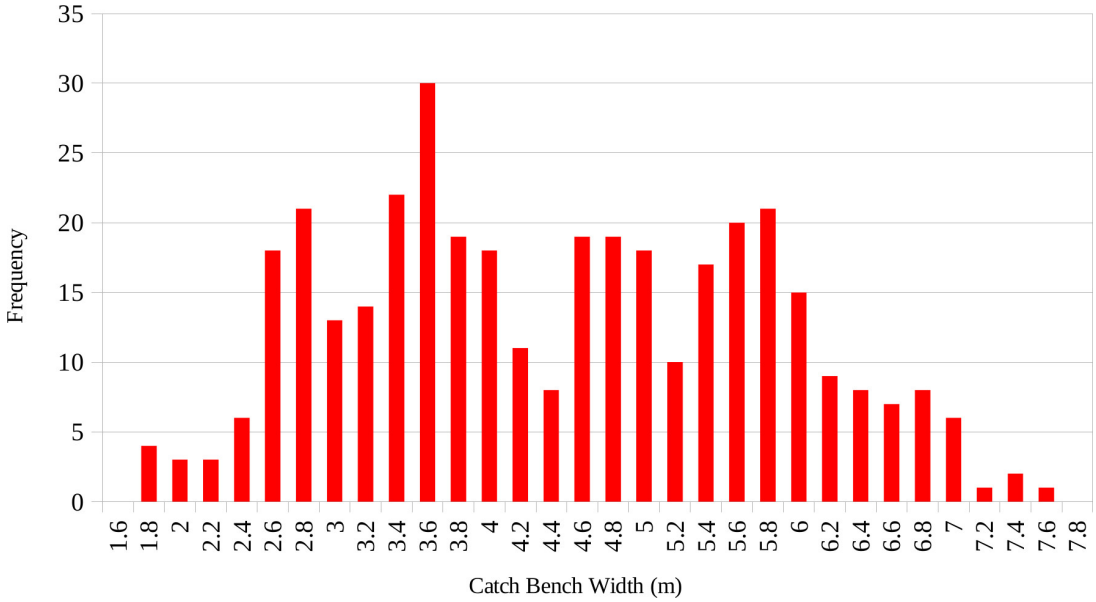

Figure 12. Catch bench analysis at Mine A. The designed catch bench width is 10 m. A total of 371 sections were used for estimating catch bench width at the surveyed location.

At Mine A, the target bench face angle is 75°. In the surveyed area, there is a significant difference between the actual and the designed bench face angle at the mine. The average bench face angle is 60°, as shown in Figure 13, where the achieved bench angle on average is 15° lower than planned (blue colour is dominant). The target angle is rarely achieved, and when it is, it is generally only at the toes of the benches. Due to the presence of steeply dipping exposed joints, some slope areas are steeper than the target angle. The result shows that blasting practices at the mine have caused significant back break, particularly towards the crest of the benches, reducing the size of the catch benches and increasing the risk of loose material falling downward. Further controls should be invested to ensure the final pit walls are better maintained.

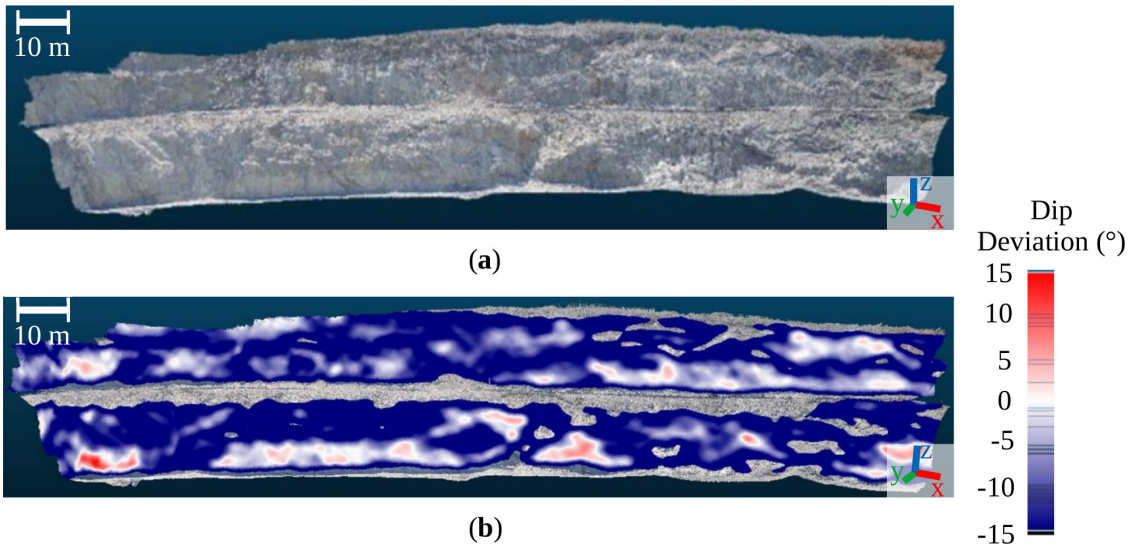

Figure 13. (**a**) Point cloud generated for Mine A and (**b**) the achieved bench face angle compared to the target bench face angle of 75°, with areas in blue lower, white ±3° of the target and red as areas above the target.

5.3. Quality Control of Pre-Split Drillholes

Pre-split holes are commonly drilled to control blast-induced pit wall damage along the final planned pit wall. The holes are typically drilled at a tight spacing along the final walls and loaded with decoupled or light charges. The charge in all the holes is blasted simultaneously, creating a tension crack between them, thereby reducing the potential damage caused by proximate production or trim blasting [8]. The final product of the pre-split blasting is a half-cast that remains on the wall. The lengths, dip and azimuth of the half-casts can be mapped using 3D point cloud models of pit walls in CloudCompare software, as shown in Figure 14. The results can then be used to conduct quality control of the pre-split drilling and allowing the provision of feedback to drillers.

With the pre-split hole mapping, it was possible to evaluate the half-cast factor (HCF) in Mine C (see C1 in Appendix A for the UAV survey details). HCF is defined as a ratio of the visible half-casts on the wall to the total drilled pre-split hole length in the same area. Identified fractures (in cyan) and half-casts (in orange) in order to calculate the P_{21} and HCF on a pit wall in Mine C can be seen in Figure 14. In addition to the half-cast factor, the deviation of the pre-split holes can be assessed by comparing the as-drilled holes' orientation (dip/azimuth) with the as-designed holes' orientation. For drill hole dip deviation assessment, the actual dip angle was subtracted from the designed dip angle to determine dip angle deviation. In this study, only the drill hole dip deviation was assessed because the azimuth of the designed pre-split holes was not available for technical reasons. The dip deviation analysis in Figure 15 shows differences of up to 10° from the pre-split holes' designed dip angle of 75°.

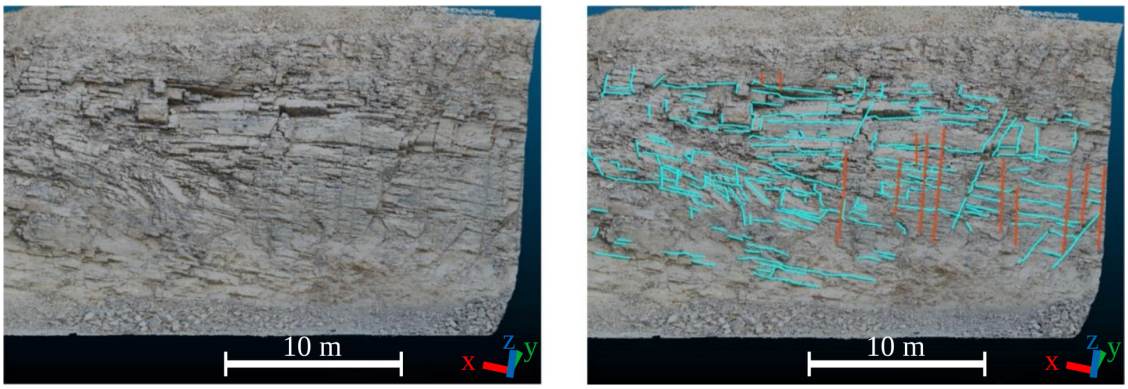

(**a**) (**b**)

Figure 14. (**a**) A 32 m section of a bench with a highly fractured rock mass in Mine C. (**b**) Mapping fractures (cyan) and half-cast pre-split holes (orange).

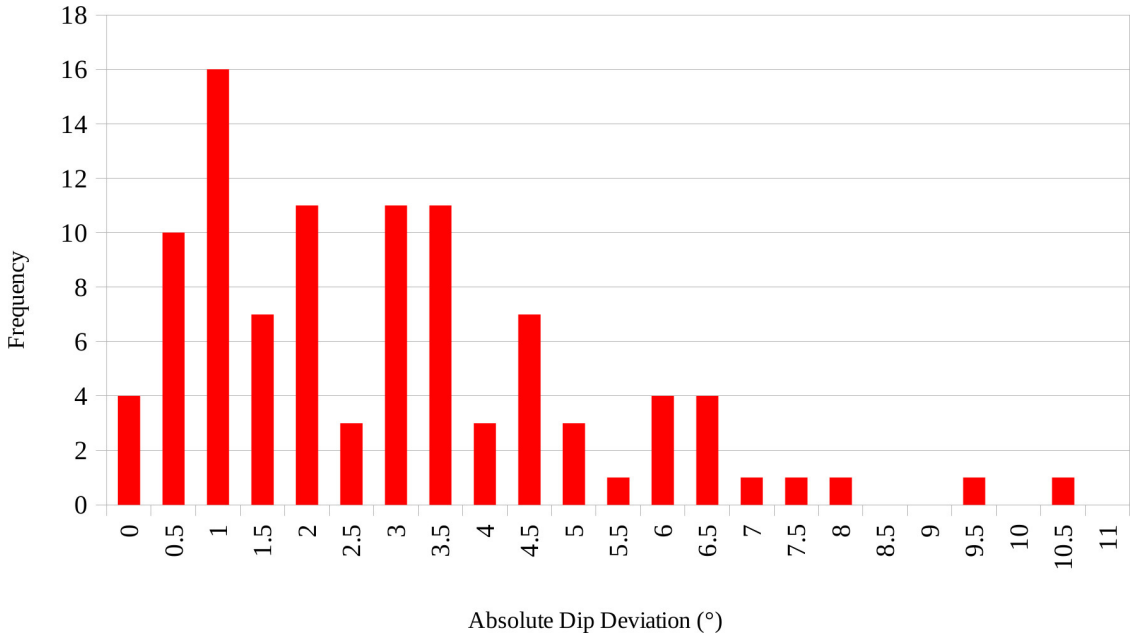

Figure 15. Histogram of pre-split holes' absolute dip deviation for Mine C assessed using the UAV photogrammetric model shown in Figure 14. A total of 100 pre-split hole measurements are included in this histogram.

Accuracy and proper alignment of the pre-split holes is critical for a mining operation, as deviation can result in uneven, over-hanging or stepped bench face conditions. Furthermore, the final bench face angle (BFA) can be affected, resulting in over-steepening or shallower than designed walls with significant economic repercussions. Measuring the accuracy of pre-split drilling orientation and the HCF can be a method for assessing the performance of pre-split blasting; however, the HCF can also be affected by the quality of the rock mass in the pit area [27]. The local geology and rock mass condition have an impact on the results of the pre-split blasting, particularly on the pre-split alignment with the dominant foliation. Birhane [60] concluded that pre-split blasting oriented parallel to foliation produced the best results, due to the presence of a plane of weakness in the same direction as tension cracking developed by the blasting.

The relationship between the quality of pre-split drilling and the local rock mass condition was further explored in this work by comparing the HCF and the pre-split deviation to the P_{21} of the rock mass. This comparison was made in four different pit walls (areas) in Mine C. This is a minimal dataset for a robust statistical analysis; however, within these areas, multiple pre-split hole

dip deviation measurements were taken. The results of the comparison, shown in Table 6, agree with Paswan et al. [27], suggesting that HCF decreases as rock mass fracture intensity P_{21} increases.

Table 6 summarizes the results obtained from virtual mapping of the photogrammetric models representing the four pit walls in Mine C including the measured areal fracture intensity (P_{21}), average pre-split hole deviation (both dip and dip direction), pre-split half-cast factor (HCF) and bench face angles achieved for the walls. In general, a higher fracture intensity (P_{21}) of rock mass resulted in higher pre-split hole deviation. Moreover, the wall with the highest fracture intensity (weaker rock mass) and pre-split hole deviation had a shallower bench face angle as a result.

Table 6. Results of virtual mapping of the point clouds representing the four different walls analysed at Mine C.

Wall	P_{21} (m^{-1})	Pre-Split Deviation (°)		HCF	Bench Face Angle (°)	
		Dip	Dip Direction		Achieved	StDev
1	0.74	4.19	4.37	0.24	66.9	4.8
2	0.28	1.29	1.23	0.41	72.7	1.6
3	0.39	1.67	1.35	0.40	74.5	3.6
4	0.32	3.11	1.85	0.64	75.5	8.7

5.4. Assessing Muck Pile Configuration

In addition to the aspects of the blast results discussed above, the following measurements are also used to assess the blasting process: muck pile profile, displacement, volume, swell and face profile [61,62]. Measuring muck pile displacement and movement is important for controlling dilution and ore loss [63]. Displacement of the muck pile is desirable, but excessive movement will cause issues for equipment productivity and grade control [61]. Several studies have shown the influence of muck pile configuration and heave achieved by a blast on diggability, a measure of the ease of digging or excavation [64–66]. According to [67], the muck pile anatomy has a significant effect on the performance of a loading machine. The swell of the muck pile can be influenced by fragmentation and has an impact on the performance of loading equipment [62]. The swell and volume of loose material are also important when keeping an inventory of loose material moved, and these can have an influence on the placement strategy used for waste piles and dumps [62]. To help evaluate blasting results, these measurements were conducted at Mine D using the UAV.

Muck pile surfaces can be measured by generating the orthophoto and DEM from images captured by the UAV. These surfaces can then be used to determine the muck pile profile, volume and swell. The DEM can also be used to measure the extent of muck pile surface displacement and heave. However, since near-surface movement does not capture all of the dynamics associated with blast movement, only using the muck pile DEM might not be sufficient for grade control [63].

In this study, two UAV surveys were conducted before (Survey D4) and after (Survey D5) a blast at Mine D to generate hillshade DEMs and DEMs (shown in Figure 16). UAV survey details are provided in Appendix A. The in situ volume of the blast location was estimated to be 42,200 m^3 using the DEM generated before the blast (Figure 16c), the planned bench design and the blast plan. Using the DEM of the muck pile (Figure 16d) and the planned bench design, the muck pile volume was estimated to be 63,100 m^3. Thus, using the pre-blast and post-blast volumes, the swell factor was calculated to be 1.49, a value that is relatively high and that can influence the productivity of the loading and hauling process at the mine. Figure 17 presents a cross-section of the blast location before and after the blast in blue and red, respectively (shown as A-A′ in Figure 16). The section shows a rock throw of ∼100 m from the bench crest and a maximum heave of ∼2 m for a 12 m bench height.

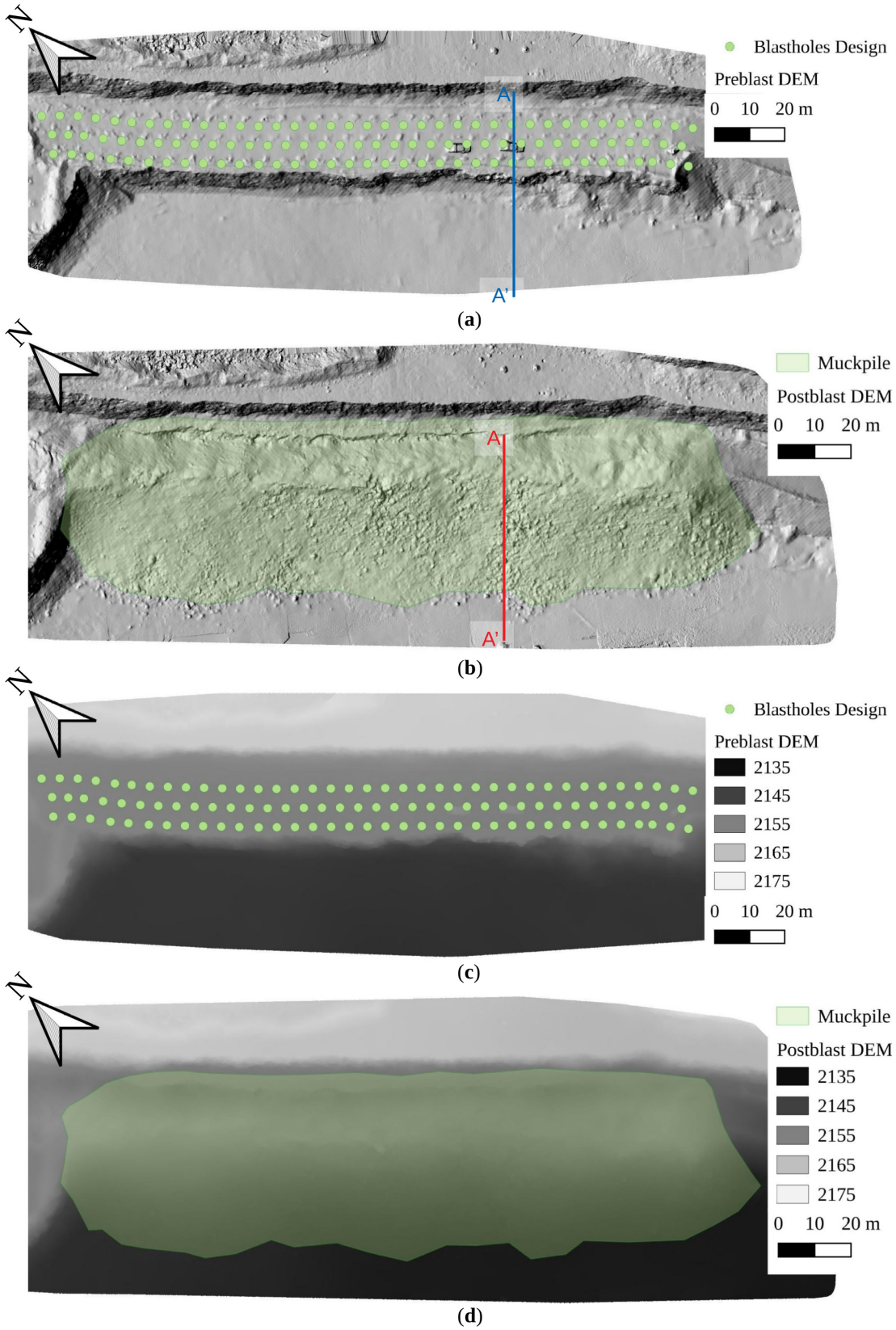

Figure 16. (**a**,**b**) Hillshade DEMs and (**c**,**d**) DEMs of the blast location at Mine D generated using UAV photogrammetry (**a**,**c**) before and (**b**,**d**) after the blast.

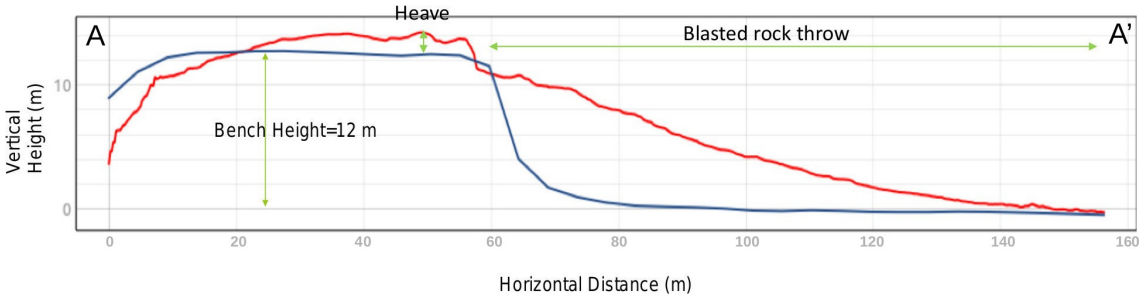

Figure 17. Section through muck pile with blue showing the pre-blast and red the post-blast DEM for the section A-A' in Figure 16.

6. Discussion

Using UAVs can significantly improve data collection at mine sites while reducing risk to personnel due to the reduced exposure in the field. The collected data can provide useful information for assessing the blasting practices at the site: the final wall conditions can be evaluated; the catch bench loss can be monitored; in situ block and blasted block size distributions can be compared; and pre- and post-blast topography can be used to calculate swell and record muck pile movement. All of the aforementioned models are highly reliant on both the quality and quantity of data, which can be improved by using a UAV. Furthermore, the data collected can be stored as a permanent visual record of the mine at a particular point in time and may be revisited as required.

For all mines studied, the UAV system was used to collect fragmentation and geotechnical data that had been previously collected with the manual method or were unavailable due to its inaccessible location. The use of drone technology can reduce the time required in the field and allows more time for post processing and analysing data. This was evident during highwall mapping at all mines. It was also shown through short flight times for the other analyses (see Appendix A). Making data permanently available for virtual mapping allows for significantly more detailed mapping. This is important because areas with intense jointing require more time and detailed mapping than is typically done using conventional techniques [68]. This has a direct impact on the study results, in particular those of DFN modelling, since more robust data are used to build the model. This information can also be used to develop site-specific relationships between the rock mass condition and the blasting outcomes.

While the advantages of using UAVs are notable, as previously discussed, there are limitations with this method. The UAV-based method was limited by the regulatory requirements that were established by the jurisdictions of the mines in this study. These regulations promoted safe operation of UAVs, but required extensive pilot training. Due to this, the time available for data collection using a UAV was constrained because each mine only had a few surveyors trained as pilots. With limited time, effective communication of model requirements was essential between the pilot and the professional conducting the analysis. This is particularly important during structural mapping where the local geology and the rock mass fracture network strongly influence the UAV-based analysis: e.g., a highly fractured rock mass needs high-resolution images (GSD) and more time for virtual mapping. If the evaluation of the required GSD is not correctly carried out, then important data can be lost when they are filtered out below the GSD. However, if the model has a very high resolution, then the area analysed by professionals can decrease significantly because of time constraints in the field and during processing. In some cases, large high-resolution models are intractable using computers available at the mines.

To highlight the differences in photogrammetric models at different GSDs, pit wall mapping was conducted for two GSDs at Mine B. Figure 18 shows the differences in the GSD for the pit wall in Mine B. Figure 18a presents the 3D model constructed using 25 images taken of the highwall, approximately 80 m tall, using the 15 mm lens (UAV Survey B1 in Appendix A). Figure 18b shows the 3D model of the highwall using a 45 mm lens and capturing 128 images at the same distance from the target (UAV Survey B3 in Appendix A). However, the point cloud covered in Figure 18b is approximately

20% of the area covered by Figure 18a. The GSD is 0.4 cm/pixel for the 45 mm lens (Figure 18b) compared to 1.5 cm/pixel with the 15 mm lens (Figure 18a). Careful consideration needs to be given to the required GSD based on the desired uses of the point cloud or orthophoto. Furthermore, the type of joints in a rock can determine whether automated algorithms for the detection of joints can be used effectively or not. The automatic joint detection is best suited for identifying clearly visible and exposed joint surfaces such as those present in Mine B. Another limitation of UAV-based highwall mapping is the impossibility to define the composition of fracture infilling and to characterize fracture roughness, which are commonly done during manual structural mapping. However, recent studies have shown promising results on using UAV photogrammetry for rock discontinuity roughness characterization [69].

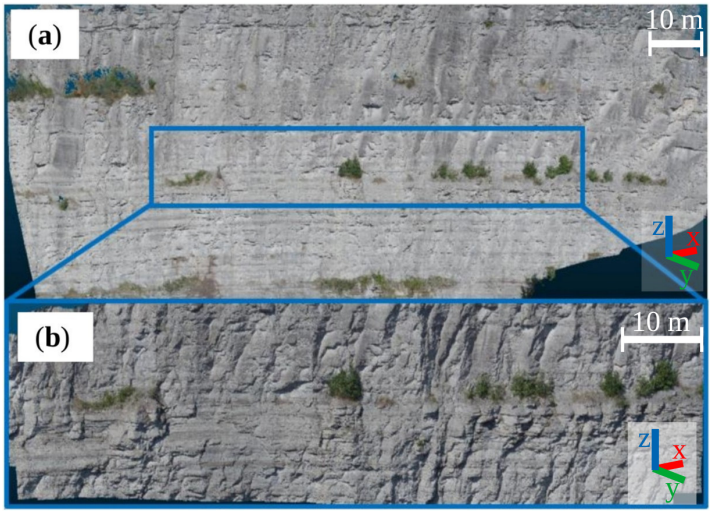

Figure 18. 3D point cloud of Mine B using (**a**) a 15 mm lens and (**b**) a 45 mm lens.

Environmental conditions also have a significant impact on the success of UAV-based methods. One major limitation is that UAV flight is limited to days with favourable weather conditions, as current UAV systems cannot operate in extreme winds, heat, rain or snow. For example, at Mine C, extreme heat limited the time available for flight to early morning and late evening. Even with this, the UAV required repair at the end of the field study due to damage caused by heat and dust accumulation. To prevent this, the UAV system should be cleaned and maintained after every flight in dusty conditions, which are present in most mines. Snow, rain and extreme winds at Mine D, located in a mountain range, limited the flight time available. To collect the desired data, the field study had to be extended until better weather conditions were available.

As the UAV-based method using photogrammetry relies on image quality, any conditions that decrease the quality of images, such as dust in the air or poor lighting condition, can reduce the effectiveness of the method. The best results are typically produced when images are collected in similar environmental conditions. For example, when lighting conditions changed, when there was glare or too much direct sunlight on the pit wall, poor results were produced. Figure 19 shows various lighting conditions and their impact on the visible image quality using the same lens, filter, focal length and camera settings (UAV Survey C1 in Appendix A). The same location in all images is identified by the green cross; however, the images were captured at different times and on different flight lines while a shadow was moving up the pit wall. The high glare environment in Figure 19a made image quality decrease, whereas the shaded environment in Figure 19b and indirect lighting environment in Figure 19c provided better quality images. Due to this, highwall mapping flights were scheduled when the wall was fully shaded or had indirect lighting to avoid glare and direct sunlight. Moreover, if the flight takes a significant time, the time of flight should be considered, and the flights should occur over the same period during the day.

Figure 19. Images captured during a single flight using the same lens, filter, focal length and camera settings. The same location on the pit wall is identified by the green cross. (**a**) High glare caused by direct sunlight, (**b**) fully shaded and (**c**) indirect lighting environments were encountered while a shadow moved up the pit wall.

7. Conclusions

The use of UAVs can aid the blast improvement process by providing valuable feedback on the blasting process while decreasing the hazards to which personnel are exposed when collecting data. The valuable feedback described in this study included pre-blast structural mapping of pit walls and IBSD estimation, assessment of drillhole alignment, identification of problem areas during the blast using high-speed photography, post-blast BBSD measurement, comparison of the theoretical and actual powder factor, assessment of blasting impact on final pit walls, quality control of pre-split drillholes and an assessment of muck pile configuration. The performance of the operation can be closely tracked without significant time requirements. Work stoppages can be avoided because remote sensing techniques are employed to collect data: a shovel does not need to stop working in order to conduct a flyover on a muck pile. Additionally, data are collected at more flexible vantage points than ground-based remote sensing. Using UAV technology, it is also possible to cover larger and commonly inaccessible areas. This is particularly useful as mining progresses deeper in open pit mines and more benches become inaccessible. If issues develop in the top benches, they can be identified and addressed in a timely manner using UAVs and digital photogrammetry to ensure safety and efficient production without significant delays.

Fragmentation assessments can be done much more frequently and integrated into routine open pit operations to improve blasting. The initial setup and flight path plan can be done simply by using the equations provided or with software provided by the UAV suppliers. Flight missions conducted at the four mine sites did not take longer than 2.5 h of flight time, saving the site personnel time in the field. However, while the UAV-based collection of raw data (images) is relatively quick compared to the ground-based and traditional methods, 3D model creation and analysis sometimes required significant time, e.g., 30.8 h for Mine A highwall model creation. Future work will focus on improving model creation and analysis to automate repetitive tasks and to decrease the human effort required to complete analysis. The data collected can also be leveraged to conduct stability analysis for geotechnical purposes, enhancing safety in the workplace while also reducing costly remediation work. The integration of UAV technology can provide continuous, safe, automated and fast acquisition of high-quality data, which can be used to achieve more efficient blasting and can highlight opportunities for further process improvement.

Author Contributions: T.B.: conceptualization, methodology, formal analysis, validation, visualization, writing, original draft preparation; F.M.: conceptualization, methodology, formal analysis, validation, writing, original draft preparation; K.E.: conceptualization, methodology, formal analysis, writing, review and editing, supervision, project administration. All authors read and agreed to the published version of the manuscript.

Funding: This research was funded by the Natural Sciences and Engineering Research Council of Canada (NSERC) Grant Number CRDPJ 508741-17 and Ontario Center of Excellence (OCE) Grant Number 28271.

Acknowledgments: The authors would like to acknowledge the support of the mining companies in conducting the field experiments.

Conflicts of Interest: The authors declare no conflict of interest.

Abbreviations

The following abbreviations are used in this manuscript:

UAV	Unmanned aerial vehicle
DEM	Digital elevation model
BBSD	Blasted block size distribution
IBSD	In situ block size distribution
GSD	Ground sampling distance
GCP	Ground control point
DFN	Discrete fracture network
P_{21}	Areal fracture intensity
P_{32}	Volumetric fracture intensity
ANFO	Ammonium nitrate/fuel oil
HCF	Half-cast factor

Appendix A

Summaries of the workflow used for UAV surveys at each mine and relevant sections are presented in Tables A1–A4.

Table A1. Workflow for Mine A.

Mine	Mine A	
Survey	**A1**	**A2**
	Equipment	
UAV	DJI Matrice 600 Pro	–
Camera	DJI Zenmuse X5 (X5)	Canon EOS 70D
Lens	DJI MFT 15 mm F1.7 ASPH	Canon EF-S 18-55mm f/3.5-5.6 IS STM
Filter	–	–
	Flight Plan	
Focal length	15.0 mm	18.0 mm
Aperture	2.5	22.6
Shutter speed	1/7692	1/1328
ISO	182	2000
Camera tilt	0°	–
Target distance	10 m	–
Front overlap	90%	–
Side overlap	70%	–
Flight speed	1 m/s	–
Area surveyed	0.9 ha (flat)	–
Flight time (h:mm)	2:16	–
Number of images	1772	1
	Model Creation	
Photogrammetry software	OpenDroneMap	–
Software settings	High resolution	–
Models constructed	Point cloud, DEM	–
Model resolution	0.2 cm/px	0.13 cm/px
Georeferencing method	EXIF data from images	Reference object
GCP count in georeferencing	0	–
Relevant section	3.1, 3.2, 5.1, 5.2	5.1

Table A2. Workflow for Mine B.

Mine	Mine B		
Survey	**B1**	**B2**	**B3**
Equipment			
UAV	DJI Matrice 600 Pro (M600P)	DJI M600P	DJI M600P
Camera	DJI Zenmuse X5 (X5)	DJI X5	DJI X5
Lens	DJI MFT 15 mm F1.7 ASPH (15 mm)	DJI 15 mm	Olympus M.Zuiko 45 mm F1.8
Filter	–	–	–
Flight Plan			
Focal length	15.0 mm	15.0 mm	45.0 mm
Aperture	16	13	16
Shutter speed	1/100	1/100	1/100
ISO	100	100	100
Camera tilt	0°	−89.90°	0°
Target distance	35 m	75 m	35 m
Front overlap	80%	85%	80%
Side overlap	80%	70%	80%
Flight speed	3 m/s	4.9 m/s	1 m/s
Area surveyed	0.3 ha (flat)	0.8 ha	0.2 ha (flat)
Flight time (h:mm)	0:04	0:02	0:10
Number of images	25	38	128
Model Creation			
Photogrammetry software	OpenDroneMap (ODM)	ODM	ODM
Software settings	High resolution	High resolution	High resolution
Models constructed	Point cloud	Orthophoto	Point cloud
Model resolution	0.9 cm/px	1.5 cm/px	0.4 cm/px
Georeferencing method	EXIF data from images	EXIF data from images	EXIF data from images
GCP count in georeferencing	0	0	0
Relevant section	3.1, 3.2, 5.1, 6	5.1	6

Table A3. Workflow for Mine C.

Mine	**Mine C**
Survey	**C1**
Equipment	
UAV	DJI Inspire 2
Camera	DJI Zenmuse X5S
Lens	Olympus M.Zuiko 45 mm F1.8
Filter	–
Flight Plan	
Focal length	45.0 mm
Aperture	6.3
Shutter speed	1/400
ISO	100
Camera tilt	0°
Target distance	100 m
Front overlap	80%
Side overlap	80%
Flight speed	3 m/s
Area surveyed	6.5 ha (flat)
Flight time (h:mm)	1:31
Number of images	610
Model Creation	
Photogrammetry software	Agisoft Metashape
Software settings	High quality, Moderate depth filtering
Models constructed	Point cloud
Model resolution	0.7 cm/px
Georeferencing method	EXIF data from the images
GCP count in georeferencing	0
Relevant section	3.1, 5.3, 6

Table A4. Workflow for Mine D.

Mine	Mine D				
Survey	**D1**	**D2**	**D3**	**D4**	**D5**
Equipment					
UAV	DJI Inspire 2 (I2)	DJI I2	DJI M600P	DJI I2	DJI I2
Camera	DJI Zenmuse X5S (X5S)	DJI X5S	Slomocam fps4000-720c -640	DJI X5S	DJI X5S
Lens	Olympus M.Zuiko 45 mm F1.8	DJI MFT 15 mm F1.7 ASPH (15 mm)	C Mount 35mm	DJI 15 mm	DJI 15 mm
Filter	Hoya Fusion Antistatic Protector (Hoya)	Hoya	–	Hoya	Hoya
Flight Plan					
Focal length	45.0 mm	15.0 mm	35.0 mm	15.0 mm	15.0 mm
Aperture	5.6	5.6	2.8	6.3	6.3
Shutter speed	1/320	1/320	1/1800	1/500	1/500
ISO	100	100	100	100	100
Camera tilt	−10.00°	−89.10°	–	−89.90°	−89.10°
Target distance	100 m	50 m	400 m	62.5 m	60 m
Front overlap	80%	85%	–	85%	85%
Side overlap	80%	70%	–	70%	70%
Flight speed	4 m/s	3.1 m/s	–	2.1 m/s	2.1 m/s
Area surveyed	2.8 ha (flat)	2.8 ha	–	1.6 ha	1.9 ha
Flight time (h:mm)	1:47	0:06	–	0:05	0:07
Number of images	1618	143	19060	68	112
Model Creation					
Photogrammetry software	Agisoft Metashape	OpenDroneMap (ODM)	–	ODM	ODM
Software settings	High quality, Moderate depth filtering	Default	–	Default	Default
Models constructed	Point cloud	Orthophoto	–	DEM	DEM
Model resolution	0.7 cm/px	1.13 cm/px	–	5 cm/px	5 cm/px
Georeferencing method	EXIF data from the images	EXIF data from the images and Poly 1 using GCPs	–	EXIF data from the images and Poly 1 using GCPs	EXIF data from the images and Poly 1 using GCPs
GCP count in georeferencing	0	5	–	6	3
Relevant section	3.1	3.3	4.1	5.4	5.4

References

1. Nielson, K.; Kristiansen, J. Blast-crushing-grinding: Optimisation of an integrated comminution system. In Proceedings of the International Symposium on Rock Fragmentation by Blasting (Fragblast), Montreal, QC, Canada, 25–29 August 1996; pp. 278–296.
2. Mosher, J. Crushing, Milling, and Grinding. In *SME Mining Engineering Handbook*, 3rd ed.; Darling, P., Ed.; Society for Mining, Metallurgy, and Exploration (SME): Englewood, CO, USA, 2011; pp. 1461–1465.
3. MacKenzie, A.S. Optimum blasting. In Proceedings of the 28th Annual Minnesota Mining Symposium, Duluth, MN, USA, 1967; pp. 181–188.
4. Scott, A. Blastability and blast design. In Proceedings of the 5th International Symposium on Rock Fragmentation by Blasting (Fragblast), Montreal, QC, Canada, 25–29 August 1996; Balkema: Montreal, QC, Canada, 1996; pp. 27–35.
5. Cunningham, C.V.B. Keynote address: Optical fragmentation assessment—A technical challenge. In *Measurement of Blast Fragmentation*; Franklin, J.A., Katsabanis, T., Eds.; Balkema: Montreal, QC, Canada, 1996; pp. 13–19.
6. Stiehr, J.F. (Ed.) *ISEE Blasters' Handbook*; International Society of Explosives Engineers (ISEE): Cleveland, OH, USA, 2011.
7. Adermann, D.; Chalmers, D.; Martin, C.; Wellink, S. High-speed video—An essential blasting tool. In Proceedings of the Fragblast, Sydney, Australia, 24–26 August 2015; pp. 471–476.
8. Read, J.; Stacey, P. (Eds.) *Guidelines for Open Pit Slope Design*; CSIRO Publishing: Clayton, Australia, 2011.
9. Singh, P.K.; Roy, M.P.; Paswan, R.K. Controlled blasting for long term stability of pit-walls. *Int. J. Rock Mech. Min. Sci.* **2014**, *70*, 388–399. doi:10.1016/j.ijrmms.2014.05.006.
10. Colomina, I.; Molina, P. Unmanned aerial systems for photogrammetry and remote sensing: A review. *ISPRS J. Photogramm. Remote Sens.* **2014**, *92*, 79–97. doi:10.1016/j.isprsjprs.2014.02.013.
11. Dash, J.P.; Watt, M.S.; Pearse, G.D.; Heaphy, M.; Dungey, H.S. Assessing very high resolution UAV imagery for monitoring forest health during a simulated disease outbreak. *ISPRS J. Photogramm. Remote Sens.* **2017**, *131*, 1–14. doi:10.1016/j.isprsjprs.2017.07.007.
12. Bamford, T.; Esmaeili, K.; Schoellig, A.P. A real-time analysis of post-blast rock fragmentation using UAV technology. *Int. J. Min. Reclam. Environ.* **2017**, *31*, 439–456. doi:10.1080/17480930.2017.1339170.
13. Sayab, M.; Aerden, D.; Paananen, M.; Saarela, P. Virtual structural analysis of Jokisivu open pit using 'structure-from-motion' Unmanned Aerial Vehicles (UAV) photogrammetry: Implications for structurally-controlled gold deposits in Southwest Finland. *Remote Sens.* **2018**, *10*, 1296. doi:10.3390/rs10081296.
14. Tziavou, O.; Pytharouli, S.; Souter, J. Unmanned Aerial Vehicle (UAV) based mapping in engineering geological surveys: Considerations for optimum results. *Eng. Geol.* **2018**, *232*, 12–21. doi:10.1016/j.enggeo.2017.11.004.
15. Ren, H.; Zhao, Y.; Xiao, W.; Hu, Z. A review of UAV monitoring in mining areas: Current status and future perspectives. *Int. J. Coal Sci. Technol.* **2019**, *6*, 320–333. doi:10.1007/s40789-019-00264-5.
16. Salvini, R.; Mastrorocco, G.; Seddaiu, M.; Rossi, D.; Vanneschi, C. The use of an unmanned aerial vehicle for fracture mapping within a marble quarry (Carrara, Italy): photogrammetry and discrete fracture network modelling. *Geomat. Nat. Hazards Risk* **2017**, *8*, 34–52. doi:10.1080/19475705.2016.1199053.
17. Francioni, M.; Salvini, R.; Stead, D.; Giovannini, R.; Riccucci, S.; Vanneschi, C.; Gullì, D. An integrated remote sensing-GIS approach for the analysis of an open pit in the Carrara marble district, Italy: Slope stability assessment through kinematic and numerical methods. *Comput. Geotech.* **2015**, *67*, 46–63. doi:10.1016/j.compgeo.2015.02.009.
18. Valencia, J.; Battulwar, R.; Naghadehi, M.Z.; Sattarvand, J. Enhancement of explosive energy distribution using UAVs and machine learning. In Proceedings of the 39th International Symposium on Application of Computers and Operations Research in the Mineral Industry (APCOM), Wroclaw, Poland, 4–6 June 2019; pp. 671–677. doi:10.1201/9780429320774-79.
19. Alvarado, M.; Gonzalez, F.; Fletcher, A.; Doshi, A. Towards the development of a low cost airborne sensing system to monitor dust particles after blasting at open-pit mine sites. *Sensors* **2015**, *15*, 19667–19687. doi:10.3390/s150819667.

20. Propeller Aerobatics Pty Ltd. What Is Ground Sample Distance (GSD) and How Does It Affect Your Drone Data? Available online: https://www.propelleraero.com/blog/ground-sample-distance-gsd-calculate-drone-data/ (accessed on 7 August 2020).
21. Langford, M.; Fox, A.; Smit, R.S. Using different focal length lenses, camera kits. In *Langford's Basic Photography*; Elsevier: Amsterdam, The Netherlands, 2010; pp. 92–113. doi:10.1016/B978-0-240-52168-8.10005-7.
22. Pix4D SA. Selecting the Image Acquisition Plan Type. https://support.pix4d.com/hc/en-us/articles/202557409-Step-1-Before-Starting-a-Project-1-Designing-the-Image-Acquisition-Plan (accessed on 29 January 2020).
23. QGIS Development Team. *QGIS Geographic Information System*; 2019. Available online: https://qgis.org/en/site/ (accessed on 9 July 2020).
24. OpenDroneMap Development Team. *OpenDroneMap*; 2019. Available online: https://www.opendronemap.org/ (accessed on 9 July 2020).
25. Agisoft LLC. *Agisoft Metashape*; Agisoft LLC.: St. Petersburg, Russia, 2019.
26. Menegoni, N.; Giordan, D.; Perotti, C.; Tannant, D.D. Detection and geometric characterization of rock mass discontinuities using a 3D high-resolution digital outcrop model generated from RPAS imagery-Ormea rock slope, Italy. *Eng. Geol.* **2019**, *252*, 145–163. doi:10.1016/j.enggeo.2019.02.028.
27. Paswan, R.K.; Roy, M.P.; Kumar, S. Blast induced damage and role of discontinuities on pre-split blasting at Rampura-Agucha Pb-Zn. In Proceedings of the NexGen Technologies for Mining and Fuel Industries, New Delhi, India, 15–17 February 2017; pp. 281–290.
28. Elmouttie, M.K.; Poropat, G.V. A method to estimate in situ block size distribution. *Rock Mech. Rock Eng.* **2012**, *45*, 401–407. doi:10.1007/s00603-011-0175-0.
29. Grenon, M.; Hadjigeorgiou, J.; Liu, Q. Quantifying in situ rock block size and resulting fragment size distributions due to blasting. *Proc. Fragblast* **1998**, *2*, 205–218. doi:10.1080/13855149809408886.
30. Latham, J.P.; Van Meulen, J.; Dupray, S. Prediction of in situ block size distributions with reference to armourstone for breakwaters. *Eng. Geol.* **2006**, *86*, 18–36. doi:10.1016/j.enggeo.2006.04.001.
31. Hadjigeorgiou, J. Where do the data come from? *Min. Technol.* **2012**, *121*, 236–247. doi:10.1179/1743286312Y.0000000026.
32. CloudCompare Development Team. *CloudCompare*; 2019. Available online: https://www.danielgm.net/cc/ (accessed on 9 July 2020).
33. Thiele, S.T.; Grose, L.; Samsu, A.; Micklethwaite, S.; Vollgger, S.A.; Cruden, A.R. Rapid, semi-automatic fracture and contact mapping for point clouds, images and geophysical data. *Solid Earth* **2017**, *8*, 1241–1253. doi:10.5194/se-8-1241-2017.
34. Dewez, T.J.B.; Girardeau-Montaut, D.; Allanic, C.; Rohmer, J. Facets: A CloudCompare plugin to extract geological planes from unstructured 3d point clouds. *Int. Arch. Photogramm. Remote Sens. Spat. Inf. Sci. ISPRS Arch.* **2016**, *41*, 799–804. doi:10.5194/isprsarchives-XLI-B5-799-2016.
35. Elmo, D.; Rogers, S.; Stead, D.; Eberhardt, E. Discrete Fracture Network approach to characterise rock mass fragmentation and implications for geomechanical upscaling. *Min. Technol.* **2014**, *123*, 149–161. doi:10.1179/1743286314Y.0000000064.
36. Lei, Q.; Latham, J.P.; Tsang, C.F. The use of discrete fracture networks for modelling coupled geomechanical and hydrological behaviour of fractured rocks. *Comp. Geotech.* **2016**, *85*, 151–176. doi:10.1016/j.compgeo.2016.12.024.
37. Dershowitz, W.S.; Einstein, H.H. Characterizing rock joint geometry with joint system models. *Rock Mech. Rock Eng.* **1988**, *21*, 21–51. doi:10.1007/BF01019674.
38. Urli, V.; Esmaieli, K. A stability-economic model for an open stope to prevent dilution using the ore-skin design. *Int. J. Rock Mech. Min. Sci.* **2016**, *82*, 71–82. doi:10.1016/j.ijrmms.2015.12.001.
39. Brzovic, A.; Rogers, S.; Webb, G.; Hurtado, J.P.; Marin, N.; Schachter, P.; Alvarez, J.; Baraona, K. Discrete fracture network modelling to quantify rock mass pre-conditioning at the El Teniente Mine, Chile. *Min. Technol.* **2015**, *124*, 163–177. doi:10.1179/1743286315Y.0000000019.
40. Rogers, S.; Elmo, D.; Webb, G.; Guajardo Moreno, C. DFN Modelling of major structural instabilities in a large open pit for end of life planning purposes. In Proceedings of the 50th US Rock Mechanics/Geomechanics Symposium, Houston, TX, USA, 26–29 June 2016; pp. 1–15.
41. Esmaieli, K.; Hadjigeorgiou, J.; Grenon, M. Capturing the complete stress–strain behaviour of jointed rock using a numerical approach. *Int. J. Num. Anal. Meth Geomech.* **2015**, *39*, 1027–1044. doi:10.1002/nag.2346.

42. Hadjigeorgiou, J.; Esmaieli, K.; Grenon, M. Stability analysis of vertical excavations in hard rock by integrating a fracture system into a PFC model. *Tunnel. Underg. Space Technol.* **2009**, *24*, 296–308. doi:10.1016/j.tust.2008.10.002.
43. Latham, J.P.; Lu, P. Development of an assessment system for the blast ability of rock masses. *Int. J. Rock Mech. Min. Sci.* **1999**, *36*, 41–55.
44. Yarahmadi, R.; Bagherpour, R.; Taherian, S.G.; Sousa, L.M. Discontinuity modelling and rock block geometry identification to optimize production in dimension stone quarries. *Eng. Geol.* **2018**, *232*, 22–33. doi:10.1016/j.enggeo.2017.11.006.
45. Elmo, D.; Stead, D.; Rogers, S. Guidelines for the quantitative description of discontinuities for use in Discrete Fracture Network Engineering. In Proceedings of the 13th ISRM International Congress of Rock Mechanics, Montreal, QC, Canada, 10–13 May 2015; p. 587.
46. Golder Associates Ltd. *FracMan7*; Golder Associates Ltd.: Toronto, ON, Canada, 2019.
47. Esmaieli, K.; Hadjigeorgiou, J.; Grenon, M. Estimating geometrical and mechanical REV based on synthetic rock mass models at Brunswick Mine. *Int. J. Rock Mech. Min. Sci.* **2010**, *47*, 915–926. doi:10.1016/j.ijrmms.2010.05.010.
48. Adebayo, B.; Mutandwa, B. Correlation of blast-hole deviation and area of block with fragment size and fragmentation cost. *Int. Res. J. Eng. Technol.* **2015**, *2*, 402–406.
49. Sanchidrián, J.A.; Segarra, P.; Ouchterlony, F.; López, L.M. On the accuracy of fragment size measurement by image analysis in combination with some distribution functions. *Rock Mech. Rock Eng.* **2009**, *42*, 95–116. doi:10.1007/s00603-007-0161-8.
50. Ouchterlony, F.; Sanchidrián, J.A. A review of development of better prediction equations for blast fragmentation. *J. Rock Mech. Geotech. Eng.* **2019**, *11*, 1094–1109. doi:10.1016/j.jrmge.2019.03.001.
51. Onederra, I.; Thurley, M.J.; Catalan, A. Measuring blast fragmentation at Esperanza mine using high-resolution 3D laser scanning. *Min. Technol.* **2014**, *124*, 34–36. doi:10.1179/1743286314y.0000000076.
52. Campbell, A.D.; Thurley, M.J. Application of laser scanning to measure fragmentation in underground mines. *Min. Technol.* **2017**, *126*, 240–247. doi:10.1080/14749009.2017.1296668.
53. Tamir, R.; Wagner, M.; Campbell, J.; Dakers, N. Utilization of aerial drones to optimize blast and stockpile fragmentation. *J. Explos. Eng.* **2017**, *34*, 6–15.
54. Bamford, T.; Esmaeili, K.; Schoellig, A.P. Evaluation of UAV system accuracy for automated fragmentation measurement. In Proceedings of the International Symposium on Rock Fragmentation by Blasting (Fragblast), Luleå, Sweden, 9–15 June 2018; pp. 715–730.
55. Leite, F.; Miranda, V.; Palangio, T. Pattern expansion optimization model based on fragmentation analysis with drone technology. In Proceedings of the International Symposium on Rock Fragmentation by Blasting (Fragblast), Luleå, Sweden, 9–15 June 2018; pp. 731–740.
56. Schenk, F.; Tscharf, A.; Mayer, G.; Fraundorfer, F. Automatic muck pile characterization from UAV images. *ISPRS Ann. Photogramm. Remote Sens. Spatial Inf. Sci.* **2019**, *IV-2/W5*, 163–170. doi:10.5194/isprs-annals-IV-2-W5-163-2019.
57. Split Engineering LLC. *Splt-Desktop: Fragmentation Analysis Software*; Split Engineering LLC: Tucson, AZ, USA, 2019. Available online: https://www.spliteng.com/products/split-desktop-software/ (accessed on 9 July 2020).
58. Latham, J.P.; Meulen, J.V.; Dupray, S. Prediction of fragmentation and yield curves with reference to armourstone production. *Eng. Geol.* **2006**, *87*, 60–74. doi:10.1016/j.enggeo.2006.05.005.
59. Kahriman, A.; Özkan, Ş.G.; Sül, O.L.; Demirci, A. Estimation of the powder factor in bench blasting from the Bond work index. *Min. Technol.* **2001**, *110*, 114–118. doi:10.1179/mnt.2001.110.2.114.
60. Birhane, M. Presplitting at Aitik Mine: Presplitting—A Case Study at Aitik Mine. Master's Thesis, Luleå University of Technology, Luleå, Sweden, 2014.
61. Thornton, D. The implications of blast-induced movement to grade control. In Proceedings of the Seventh International Mining Geology Conference, Perth, Australia, 17–19 August 2009.
62. Berkhimer, E.N. Selection and Sizing of Excavating, Loading, and Hauling Equipment. In *SME Mining Engineering Handbook*, 3rd ed.; Darling, P., Ed.; SME: Englewood, CO, USA, 2011; pp. 931–939.
63. Bhander, S. *Engineering Rock Blasting Operations*; A. A. Balkema: Rotterdam, The Netherlands, 1997.
64. Brunton, I.; Thornton, D.; Hodson, R.; Sprott, D. Impact of blast fragmentation on hydraulic excavator dig time. In Proceedings of the 5th Large Open Pit Mining Conference, Kalgoorlie, Australia, 3–5 November 2003.

65. Osanloo, M.; Hekmat, A. Prediction of shovel productivity in the Gol-e-Gohar iron mine. *J. Min. Sci.* **2005**, *41*, 177–184. doi:10.1007/s10913-005-0081-5.
66. Singh, S.P.; Narendrula, R.; Duffy, D. Influence of blasted muck on the performance of loading equipment. In Proceedings of the 3rd EFEE Conference on Explosives and Blasting, Brighton, UK, 13–16 September 2005.
67. Singh, S.P.; Narendrula, R. Factors affecting the productivity of loaders in surface mines. *Int. J. Min. Reclam. Environ.* **2006**, *20*, 20–32. doi:10.1080/13895260500261574.
68. Tuckey, Z.; Paul, J.; Price, J. Discontinuity survey and brittle fracture characterisation in open pit slopes using photogrammetry. In Proceedings of the First Asia Pacific Slope Stability in Mining Conference, Brisbane, Australia, 6–8 September 2016; Dight, P.M., Ed.; Australian Centre for Geomechanics: Perth, Australia, 2016; pp. 587–600.
69. Salvini, R.; Vanneschi, C.; Coggan, J.S.; Mastrorocco, G. Evaluation of the use of UAV photogrammetry for rock discontinuity roughness characterization. *Rock Mech. Rock Eng.* **2020**, *53*, 3699–3720. doi:10.1007/s00603-020-02130-2.